Rapid Perturbation Growth on Spatially and Temporally Varying Oceanic Flows Determined Using an Adjoint Method: Application to the Gulf Stream

ANDREW M. MOORE

CSIRO Division of Atmospheric Research, Mordialloc, Victoria, Australia

BRIAN F. FARRELL

Department of Earth and Planetary Sciences, Harvard University, Cambridge, Massachusetts

(Manuscript received 29 April 1992, in final form 6 October 1992)

ABSTRACT

The stability of the Gulf Stream flow predicted by a nonlinear quasigeostrophic model is examined by employing an iterative method, which uses both the tangent linear equations and the adjoint tangent linear equations of the quasigeostrophic model. The basic state flow is the model's representation of the Gulf Stream as observed during January and February 1988. The growth of perturbation energy is examined as a measure of disturbance growth and linear perturbations are found that are optimal in the sense that they maximize the growth of perturbation energy. The structures of optimal perturbations are compared with the structure of the normal modes. The optimal perturbations are found to be more localized and to grow much more rapidly than the normal modes.

Optimal perturbations are of interest because they can be used to place tight constructive upper bounds on the growth of perturbations to ocean currents such as the Gulf Stream, and they provide valuable information about the predictability of such flows.

Initially the stability of a basic-state flow that is stationary in time is considered. The inclusion of time dependence in the basic state is straightforward using the method adopted here, and it is found that the time evolution of the basic-state flow can have a large influence on the structure and preferred location of the optimal perturbation.

1. Introduction

Stability analysis of atmospheric and oceanic flows has traditionally involved indentifying the modes of maximum exponential growth (e.g., Eady 1949; Charney 1947; Pedlosky 1979; Gill 1982). While modal analysis has enjoyed a fair degree of success in explaining certain aspects of the observed atmospheric circulation (e.g., Frederiksen 1982, 1986, 1989; Frederiksen and Webster 1988), modal growth rates are significantly reduced by realistic dissipation (e.g., Pedlosky 1979; Valdes and Hoskins 1988; Farrell 1985), and modal analyses often fall short of explaining the rapid growth rates associated with cyclogenesis. Furthermore, in the atmosphere, normal modes derived from observed flows are generally global in nature, while in reality disturbances are often highly localized, at least in their early stages.

An alternative to the traditional modal approach to stability analysis has recently been advanced based on demonstrations that rapid transient growth can arise from nonmodal disturbances (Farrell 1985). Initial growth of nonmodal disturbances occurs even in examples for which the basic-state flow field supports no individual growing normal modes. Under these circumstances, the energy released by transient growth can be channeled into neutral or lightly damped modes, which can attain large amplitude by this mechanism (Farrell 1988).

A convenient property of unstable modal solutions is that they grow at the same rate with respect to all norms. However, in general, normal modes are not orthogonal, except in the special case of self-adjoint systems, and it can be shown that the structure of the disturbance required to optimally excite a normal mode is not the same as that of the normal mode itself (Farrell 1989). Optimal structures can be found for the general disturbances for which the growth in a chosen norm is maximized; for example, Farrell (1989) found optimal perturbations that maximize the growth of quasigeostrophic perturbation root-mean-square streamfunction amplitude and perturbation energy over synoptic time periods in a baroclinic atmosphere. These optimal perturbations were found to have growth rates and structures consistent with the cyclogenesis mechanism described by Petterssen and Smebye (1971)

Corresponding author address: Dr. Andrew M. Moore, BMRC, GPO Box 1298K, Melbourne 3001 Australia.

in which an upper-level disturbance is observed to overtake a lower-level depression in a vertically sheared flow. Optimal perturbations characteristically have specific structures that develop in time and become oriented in such a way so as to maximize growth in the chosen norm over the given time interval.

One important reason for studying optimal perturbations is to place an upper limit on the growth that can occur for a given flow configuration. The rapid growth associated with optimal perturbations is also relevant to assessing predictability in numerical models of both the atmosphere and ocean. It is well known that small differences in the initial conditions of atmospheric general circulation models can give rise to model forecasts that diverge rapidly in time (e.g., Lorenz 1965, 1969a,b, 1982; Charney et al. 1966; Hoffman and Kalnay 1983; Palmer 1988). While it is often assumed that the most rapidly growing normal mode is the most important disturbance to study, optimal perturbations that grow more rapidly than the most rapidly growing mode over the forecast time can be found, which may be more important in limiting predictability (Lacarra and Talagrand 1988; Farrell 1990). The study of optimal perturbations can yield information about preferred locations and mechanisms of model forecast error growth.

Recently, Farrell and Moore (1992, hereafter FM) employed an iterative method for finding optimal perturbations to oceanic flows using a nonlinear model, the associated tangent linear model, and its adjoint, in an extension of the method used by Lacarra and Talagrand (1988). Farrell and Moore demonstrate this method in a periodic zonal channel and consider pure barotropic, pure baroclinic, and mixed shear instabilities that develop on a Gaussian jet, with dimensions and flow parameters similar to those of the observed Gulf Stream. In this paper, we extend the method of FM and apply it to a more realistic Gulf Stream configuration using the Harvard open-ocean quasigeostrophic model that has been used for forecasting the Gulf Stream (Robinson et al. 1989a,b). We examine the stability of a typical Gulf Stream configuration by finding the most rapidly growing normal mode and, in addition, a series of optimal perturbations that maximize the growth of physically meaningful norms. We begin by considering the stability of stationary basic states and then extend our analyses to nonlinear time-dependent basic states.

The dynamics of ocean eddy formation are not fully understood, and the influence of eddies on the large-scale ocean circulation is largely unknown. Theoretical, modeling, and observational studies aimed at increasing our understanding of eddy formation and the stability of ocean flows have been undertaken in the context of both ocean currents (e.g., Hauriwitz and Panofsky 1950; Pedlosky 1964; Tareev 1965; Orlanski and Cox 1973; Killworth 1980; Ikeda 1981; Tracey and Watts 1986) and the open ocean (e.g., Robinson and McWilliams 1974; Gill et al. 1974; MODE Group 1978). The Gulf Stream is often considered to be an archetypal western boundary current, and previous studies have focused either on the influence that different parameter ranges have on Gulf Stream stability (Orlanski and Cox 1973; Holland and Haidvogel 1980) or on the dynamics of particular events such as meander and eddy formation (Ikeda 1981; Robinson et al. 1988). While the example considered here was chosen to illustrate a method of stability analysis, it also demonstrates the power of the tangent linear model and its adjoint as an analysis tool for examining the stability of complex mixed barotropic and baroclinic flow fields.

The linear theory of optimal perturbations is briefly reviewed in section 2. The quasigeostrophic system of equations, their associated tangent linear equations, the adjoint tangent linear equations, and their methods of solution are described in section 3. The perturbation energy equation for the open-ocean model is derived in section 4 and is used to analyze the modes and optimal perturbations found later. Section 5 describes the model domain and the Gulf Stream flow fields used in this study. The fastest-growing modes and optimal perturbations on a Gulf Stream flow, which is assumed stationary in time, are described in section 6. The condition of stationarity is relaxed in section 7, and optimal perturbations and modes are found on spatially and temporally varying Gulf Stream flows. Concluding remarks can be found in section 8.

2. Linear theory of optimal excitation

First we must decide what we mean when we say that a perturbation is optimal (i.e., whether the perturbation is to maximize the growth of perturbation energy, or some other quantity such as the squared perturbation streamfunction amplitude or perturbation potential enstrophy). In this section a method is described for obtaining the optimal excitation for a particular flow regime, which involves using the adjoint of the physical system under consideration. A number of groups (NCAR, NMC, ECMWF, METEO-France, and AOML) are currently developing the adjoints of atmospheric or oceanic general circulation models to be used for data assimilation purposes. However, we will demonstrate that these adjoint models can also be used for the study of instabilities, and for investigating the predictability of atmospheric and oceanic forecasting systems, a potentially very powerful application of such models. A brief discussion of perturbation equations and their properties follows; a more extensive development can be found in Le Dimet and Talagrand (1986) and Lacarra and Talagrand (1988).

Consider a nonlinear system with state vector ψ:

$$\frac{d\psi}{dt} = L(\psi). \tag{1}$$

The solution $\psi(t)$ corresponds to a trajectory in phase

space uniquely determined by an initial condition $\psi(0)$. Perturbations to this initial condition result in deviations from the original trajectory, so that the system follows a new trajectory $\tilde{\psi}(t) = \psi(t) + \delta\psi(t)$. Sufficiently small deviations $\delta\psi(t)$ are obtained by integrating the tangent linear perturbation equation:

$$\frac{d\delta\psi}{dt} = \mathbf{A}(t)\delta\psi, \tag{2}$$

obtained by linearizing (1) about the solution $\psi(t)$. This system relates deviations from the original trajectory to perturbations $\delta\psi(0)$ imposed at the initial time $t = 0$. In general, $\mathbf{A}(t)$ is a linear but nonautonomous operator; it is autonomous if ψ is a stationary solution of (1). There is a unique operator, called the propagator (also referred to as the resolvent by Le Dimet and Talagrand 1986), that connects the initial conditions at time $t = 0$ to the solution at a later time t:

$$\delta\psi(t) = \mathbf{R}(t, 0)\delta\psi(0). \tag{3}$$

Before we can define the adjoint of (3), we must first define an inner product, $\langle\psi, \phi\rangle$. Using this inner product, we can define a norm that is a measure of the relative magnitude of solutions,

$$|\psi| = \langle\psi, \psi\rangle^{1/2}. \tag{4}$$

The choice of an inner product and associated norm is consequential and should reflect some physically meaningful measure that sheds light on a particular aspect of perturbation development. All of the norms of a single normal mode will grow or decay at the same exponential rate, and any norm is as good as another for assessing the growth of such a mode. This is not the case for optimal perturbations, and the determined structure as well as the growth rate of these perturbations depends on the norm chosen. We reserve our choice of inner product and norm appropriate for this study until section 3. Our present discussion is sufficiently general to encompass any choice of norm and inner product.

For any linear operator $\mathbf{M}$, there exists an adjoint operator $\mathbf{M}^*$, such that

$$\langle\psi, \mathbf{M}\phi\rangle = \langle\mathbf{M}^*\psi, \phi\rangle \tag{5}$$

(Courant and Hilbert 1962). In particular, there exists for the propagator ($\mathbf{R}$) of our system an adjoint propagator ($\mathbf{R}^*$) with the property

$$\begin{aligned}\langle\delta\psi(t), \delta\psi(t)\rangle &= \langle\mathbf{R}(t, 0)\delta\psi(0), \mathbf{R}(t, 0)\delta\psi(0)\rangle \\ &= \langle\mathbf{R}^*(0, t)\mathbf{R}(t, 0)\delta\psi(0), \delta\psi(0)\rangle. \end{aligned}\tag{6}$$

The adjoint propagator is obtained from $\mathbf{S}(0, t)$, the propagator of the adjoint of (2); that is,

$$\frac{d\delta\psi^*}{dt} = -\mathbf{A}^*(t)\delta\psi^*, \tag{7}$$

where $\mathbf{A}^*(t)$ is the adjoint of $\mathbf{A}(t)$. It is easy to show that the inner product of any solution of the perturbation equation (2) with a solution of the associated adjoint equation (7) is constant, and particularly,

$$\langle\delta\psi(0), \mathbf{S}(0, t)\delta\psi^*(t)\rangle = \langle\mathbf{R}(t, 0)\delta\psi(0), \delta\psi^*(t)\rangle. \tag{8}$$

Recalling the definition of the adjoint (5), inspection of (8) shows that the adjoint of the propagator of the perturbation equation between time 0 and t is the propagator of the adjoint equation between time t and 0. Operationally, the perturbation adjoint over a time interval t can be obtained by integrating its adjoint equation backward in time over the same interval.

We are now equipped to find the most rapidly growing perturbation in the norm of the bracket inner product (4) over a specified time interval. We define a squared amplification factor λ using (4) over a time interval τ as

$$\lambda = \frac{\langle\mathbf{R}(\tau, 0)\delta\psi(0), \mathbf{R}(\tau, 0)\delta\psi(0)\rangle}{\langle\delta\psi(0), \delta\psi(0)\rangle}. \tag{9}$$

Equation (9) can be rewritten using the property of the adjoint (5) as

$$\lambda = \frac{\langle\mathbf{R}^*(0, \tau)\mathbf{R}(\tau, 0)\delta\psi(0), \delta\psi(0)\rangle}{\langle\delta\psi(0), \delta\psi(0)\rangle}. \tag{10}$$

The largest eigenvalue of the composite operator $\mathbf{R}_\tau^*\mathbf{R}_\tau$, where $\mathbf{R}_\tau = \mathbf{R}(\tau, 0)$, will be associated with the most rapidly growing eigenvector of the norm $\langle\delta\psi, \delta\psi\rangle$. The entire spectrum of the operator $\mathbf{R}_\tau^*\mathbf{R}_\tau$ is of interest if we wish to study the growth of variance in the system (Lorenz 1965; Farrell 1990), but for the present purposes we restrict our attention to the largest λ and its associated eigenfunction. These can be obtained by a simple application of the power method, suggested by inspection of (10), as follows. First, integrate the first-guess $\delta\psi(0)$ forward in time from $t = 0$ to $t = \tau$. Second, integrate the result backward in time with the adjoint equation from $t = \tau$ to $t = 0$, and iterate this procedure until convergence to the perturbation of largest λ is isolated. This procedure is constructive in that it provides both the amplification factor $\lambda^{1/2}$ and the most rapidly growing perturbation. Clearly, the form of the adjoint $\mathbf{R}^*$ and the ultimate meaning of λ depend on our choice of inner product. We must choose carefully an inner product that defines a physically meaningful norm.

If we restrict attention to stationary solutions of (1), the perturbation equation (2) is autonomous, and the most rapidly growing mode is found by integrating forward a random initial $\delta\psi$ until exponential growth is obtained and the leading eigenfunction emerges. The most effective excitation of the most rapidly growing normal mode follows from the biorthogonality between the normal modes of the perturbation equation and the normal modes of its adjoint. Recalling the property of adjoints (5), and that the spectrum of an operator is identical to that of its adjoint, a biorthogonality re-

lation can be found so that for properly normalized $\delta\psi_i^*$ and $\delta\psi_j$ (Courant and Hilbert 1962)

$$\langle \delta\psi_i^*, \delta\psi_j \rangle = \delta_{ij}. \tag{11}$$

An arbitrary initial perturbation ϕ can be projected onto the modes:

$$\phi = \sum_{i=1}^{N\to\infty} \alpha_i \delta\psi_i, \tag{12}$$

and excitation of the jth mode α_j is found using (11):

$$\alpha_j = \frac{\langle \delta\psi_j^*, \phi \rangle}{\langle \delta\psi_j^*, \delta\psi_j \rangle}. \tag{13}$$

It follows from the Cauchy–Schwarz inequality that the maximum α_j results from choosing ϕ to be the adjoint of the target normal mode. While for self-adjoint systems the optimal strategy for exciting a normal mode is to introduce a perturbation with the structure of that mode, this is not the case for non-self-adjoint systems.

3. The tangent linear model and adjoint

Our investigation will be restricted to oceanic flow fields described by the quasigeostrophic equations of motion, but the method described here is not restricted to quasigeostrophic systems and can be applied to any dynamical system. The numerical model that we have used is based on the Harvard University quasigeostrophic open ocean model described in detail by Haidvogel et al. (1980), Miller et al. (1981), and Robinson and Walstad (1987). Only a brief summary of the model is presented here, so the interested reader should consult the above references for further information.

The numerical model solves the nondimensional quasigeostrophic equations of motion for streamfunction (ψ) and vorticity (ζ) given by

$$\frac{\partial \zeta}{\partial t} + \alpha J(\psi, \zeta) + \beta \frac{\partial \psi}{\partial x} + F_s(\zeta) = 0 \tag{14}$$

$$\nabla_H^2 \psi + \Gamma^2 \frac{\partial}{\partial z}\left(\sigma \frac{\partial \psi}{\partial z}\right) - \zeta = 0, \tag{15}$$

subject to the surface and bottom boundary conditions,

$$\Gamma^2 \sigma \frac{\partial}{\partial t}\left(\frac{\partial \psi}{\partial z}\right) + \alpha\sigma\Gamma^2 J\left(\psi, \frac{\partial \psi}{\partial z}\right) + w + F_s\left(\sigma \frac{\partial \psi}{\partial z}\right) = 0 \quad \text{at} \quad z = 0 \quad \text{and} \quad z = -H, \tag{16}$$

where $F_s(\zeta)$ is dissipation of vorticity ζ applied in the form of a Shapiro filter of eighth order (Shapiro 1970). The Jacobian operator J is defined as

$$J(\psi, \zeta) = \frac{\partial \psi}{\partial x}\frac{\partial \zeta}{\partial y} - \frac{\partial \psi}{\partial y}\frac{\partial \zeta}{\partial x},$$

and the nondimensional parameters are given by

$$\alpha = \frac{V_0 t_0}{D}; \quad \beta = \beta_0 D t_0; \quad \Gamma^2 = \frac{f_0^2 D^2}{N_0^2 H^2}; \quad \sigma = \frac{N_0^2}{N^2}$$

$$N^2 = \frac{-g}{\rho}\frac{\partial \rho}{\partial z}; \quad f_0 = 2\Omega \sin\Theta_0,$$

where V_0, t_0, D, and H are the scalings used for velocity, time, horizontal distance, and height in the vertical, respectively; β_0 and N_0^2 are the scalings for the meridional gradient β of the Coriolis parameter and the buoyancy frequency N^2; Θ is the central latitude of the model domain; and Ω is the angular velocity of the earth. The values of these parameters appropriate for the Gulf Stream (see Robinson et al. 1988) are

$$V_0 = 0.4 \text{ m s}^{-1}, \quad t_0 = 4 \text{ days}, \quad D = 40 \text{ km},$$
$$H = 700 \text{ m}, \quad \Theta_0 = 38.3°\text{N}, \quad N_0^2 = 2 \times 10^{-5} \text{ s}^{-2}$$
$$f_0 = 9.3 \times 10^{-5} \text{ s}^{-1}, \quad \beta_0 = 2 \times 10^{-11} \text{ m s}^{-1}. \tag{17}$$

In Eq. (16), w is the vertical ageostrophic velocity due either to wind-stress forcing at the surface or to the presence of bottom topography. In what follows, we will assume a flat bottom and no wind-stress forcing. Equations (14), (15), and (16) are solved in an open domain, with four open boundaries. At these boundaries the open boundary conditions of Charney et al. (1950) are applied: ψ is specified everywhere on the open boundary, while ζ is specified only at inflow points.

In order to cast the problem in the framework of section 2, we require the tangent linear equations associated with (14) and (15) and their appropriate boundary conditions. The first-order equations that describe the evolution of perturbations $\delta\psi$ on a basic-state flow field ψ are

$$\frac{\partial \delta\psi}{\partial t} + \alpha L^{-1} J(\psi, L\delta\psi) + \alpha L^{-1} J(\delta\psi, L\psi) + \beta L^{-1}\frac{\partial \delta\psi}{\partial x} + L^{-1} F_s(L\delta\psi) = 0, \tag{18}$$

$$\Gamma^2\sigma\frac{\partial}{\partial t}\left(\frac{\partial \delta\psi}{\partial z}\right) + \alpha\sigma\Gamma^2 J\left(\psi, \frac{\partial \delta\psi}{\partial z}\right) + \alpha\sigma\Gamma^2 J\left(\delta\psi, \frac{\partial \psi}{\partial z}\right) + F_s\left(\sigma\frac{\partial \delta\psi}{\partial z}\right) = 0 \quad \text{at} \quad z = 0 \quad \text{and} \quad z = -H, \tag{19}$$

where the operator L is defined as

$$L = \nabla_H^2 + \Gamma^2 \frac{\partial}{\partial z}\left(\sigma \frac{\partial}{\partial z}\right). \tag{20}$$

In our fully open domain, we will assume that perturbations occur only in the interior of the domain; that is to say, $\delta\psi = 0$ at all open boundaries. In addition, we will assume that any vorticity perturbations $\delta\zeta = L\delta\psi$ advected by the basic flow ψ exit the domain at

boundary points where the basic flow is directed outside of the domain. At such points, $\delta\zeta$ is unconstrained and does not need to be specified. At boundary points where the basic-state flow is directed into the model domain, we will assume that no vorticity perturbations enter the domain from outside, in which case $\delta\zeta = 0$ at these points. These boundary conditions will be a good approximation to the true open boundary conditions for the perturbation equations over times comparable to that taken by a disturbance to be advected through the domain. For the Gulf Stream domain discussed later, this time is $\sim$10 days. For time periods longer than this, disturbances will reach the boundary, and so the influence of the flow outside of the model domain will be important.

In order to derive the adjoint of Eq. (18) subject to (19), we must choose an inner product over the domain of interest that yields a physically meaningful norm for use as a measure of perturbation growth. To this end, we define

$$\langle \psi, \phi \rangle = -\int_{-l_x}^{l_x}\int_{-l_y}^{l_y}\int_{-H}^{0} \psi L\phi dxdydz, \qquad (21)$$

where l_x, l_y, and $-H$ define the horizontal and vertical extent of the domain of interest. Using (5) and (21), we can derive the adjoint of (18); namely,

$$\frac{\partial \delta\psi^*}{\partial t} + \alpha J(\psi, \delta\psi^*) + \alpha L^{-1}J(\delta\psi^*, L\psi) + \beta L^{-1}\frac{\partial \delta\psi^*}{\partial x} + LF_s^*(L^{-1}\delta\psi^*) = 0. \qquad (22)$$

On the boundaries, the following boundary integral terms result:

$$I_x = \int_{-l_y}^{l_y}\int_{-H}^{0}\left[-\alpha\delta\psi^*\frac{\partial\psi}{\partial y}\delta\zeta + \delta\psi\frac{\partial}{\partial x}\left(\frac{\partial\delta\psi^*}{\partial t} + \alpha J(\psi, \delta\psi^*)\right) + \delta\psi\delta\psi^*\frac{\partial\Pi_0}{\partial y} - \frac{\partial\delta\psi}{\partial x}\left(\frac{\partial\delta\psi^*}{\partial t} + \alpha J(\psi, \delta\psi^*)\right)\right]_{-l_x}^{l_x} dydz$$

$$I_y = \int_{-l_x}^{l_x}\int_{-H}^{0}\left[-\alpha\delta\psi^*\frac{\partial\psi}{\partial x}\delta\zeta + \delta\psi\frac{\partial}{\partial y}\left(\frac{\partial\delta\psi^*}{\partial t} + \alpha J(\psi, \delta\psi^*)\right) + \delta\psi\delta\psi^*\frac{\partial\Pi_0}{\partial x} - \frac{\partial\delta\psi}{\partial y}\left(\frac{\partial\delta\psi^*}{\partial t} + \alpha J(\psi, \delta\psi^*)\right)\right]_{-l_y}^{l_y} dxdz$$

$$I_z = \int_{-l_x}^{l_x}\int_{-l_y}^{l_y}\left[\Gamma^2\sigma\delta\psi\frac{\partial}{\partial z}\left(\frac{\partial\delta\psi^*}{\partial t} + \alpha J(\psi, \delta\psi^*)\right) - \Gamma^2\sigma\frac{\partial\delta\psi}{\partial z}\left(\frac{\partial\delta\psi^*}{\partial t} + \alpha J(\psi, \delta\psi^*)\right)\right]_{-H}^{0} dxdy, \qquad (23)$$

where $\Pi_0 = \zeta + \beta y$ is the basic-state potential vorticity. In order to satisfy the definition of the adjoint (5), we require that the boundary integrals I_x, I_y, and I_z vanish. The boundary conditions for the tangent linear equation given above can be expressed as

$$\delta\psi = 0 \quad \text{at} \quad x = l_x \quad \text{and} \quad x = -l_x;$$

$$\delta\psi = 0 \quad \text{at} \quad y = l_y \quad \text{and} \quad y = -l_y;$$

$$\frac{\partial\delta\psi}{\partial z} = 0 \quad \text{at} \quad z = 0 \quad \text{and} \quad z = -H;$$

$\delta\zeta = 0$ when $\partial\psi/\partial x$ and $\partial\psi/\partial y$ imply inflow.

To ensure that $I_x = I_y = I_z = 0$, we require the following boundary conditions for the adjoint equation (22):

$$\frac{\partial\delta\psi^*}{\partial t} + \alpha J(\psi, \delta\psi^*) = 0 \text{ at } x = l_x \text{ and } x = -l_x;$$

$$\frac{\partial\delta\psi^*}{\partial t} + \alpha J(\psi, \delta\psi^*) = 0 \text{ at } y = l_y \text{ and } y = -l_y;$$

$$\frac{\partial}{\partial z}\left[\frac{\partial\delta\psi^*}{\partial t} + \alpha J(\psi, \delta\psi^*)\right] = 0 \text{ at } z = 0 \text{ and } z = -H;$$

$\delta\psi^* = 0$ when $\partial\psi/\partial x$ and $\partial\psi/\partial y$ imply outflow.

The identity (5) requires that the inner product of any solution of the tangent linear equations and adjoint equations be time invariant; that is,

$$\frac{\partial}{\partial t}\langle \delta\psi^*, \delta\psi \rangle = 0. \qquad (24)$$

Consider now the inner product of $\delta\psi$ with itself; namely,

$$\langle \delta\psi, \delta\psi \rangle = -\int_{-l_x}^{l_x}\int_{l_y}^{l_y}\int_{-H}^{0} \delta\psi L\delta\psi dxdydz. \qquad (25)$$

Integration by parts and application of the boundary conditions on $\delta\psi$ yields

$$\langle \delta\psi, \delta\psi \rangle = \int_{-l_x}^{l_x}\int_{-l_y}^{l_y}\int_{-H}^{0}\left(\frac{\partial\delta\psi}{\partial x}\right)^2 + \left(\frac{\partial\delta\psi}{\partial y}\right)^2 + \Gamma^2\sigma\left(\frac{\partial\delta\psi}{\partial z}\right)^2 dxdydz. \qquad (26)$$

The right-hand side of Eq. (26) is twice the integral of the total energy of the perturbation (δE).

Using Eq. (25) the growth factor λ of Eq. (10) will be a measure of the growth of perturbation energy where $\mathbf{R}_\tau$ is the propagator of Eq. (18) and $\mathbf{R}_\tau^*$ is the propagator of Eq. (22). Even though the adjoint model (22) has been derived using an inner product that yields the perturbation energy norm (26), the adjoint equation (22) can generally be used to find optimal perturbations for other quadratic norms of $\delta\psi$ by making a suitable transformation of the adjoint variables.

The nonlinear quasigeostrophic equations. (14)–(16) were discretized in space on an Arakawa B grid (Arakawa and Lamb 1977) with a grid spacing of 15 km and solved numerically using the finite element method

of Fix (1975). There were four model levels in the vertical, and ψ and ζ were calculated at depths of 150 m, 450 m, 800 m, and 2750 m. The model was discretized in time using an Adams–Bashford scheme and a time step of 45 minutes. The model geometry will be described later in relation to the Gulf Stream basic-state flow field.

The tangent linear equation (18) and the adjoint equation (22) were discretized and solved in an identical manner to the fully nonlinear equations. The adjoint numerical model was, in fact, derived from the finite difference form of the model equations using the method described by Thacker (1990) so as to yield an exact adjoint of the forward model in finite difference space. The adjoint numerical model is described in more detail by Moore (1991).

Following the procedure outlined in section 2, we have used the tangent linear model and its adjoint to find the largest eigenvalue (i.e., corresponding to growth), and associated eigenvector, of the discretized form of the operator $\mathbf{R}_\tau^*\mathbf{R}_\tau$ of Eq. (10). The procedure is iterative as follows: we first integrated the tangent linear equations (18) and (19) forward in time from $t = 0$ to $t = \tau$ starting from an arbitrary first-guess field $\delta\psi_1(0)$, where the subscript 1 refers to the first iteration. The first-guess field usually takes the form of random noise. The adjoint equation (22) is then integrated backwards in time from $t = \tau$ to $t = 0$ with initial conditions $\delta\psi^\dagger(\tau) = \delta\psi_1(\tau)$. The result $\delta\psi^\dagger(0)$ then becomes the initial condition for the next forward iteration of the tangent linear model [i.e., $\delta\psi_2(0) = \delta\psi^\dagger(0)$], and the forward–backward integration is repeated many times. As the iteration proceeds, the eigenfunction of the energy operator with the largest growth emerges from the initial first-guess field $\delta\psi_1(0)$ and dominates the tangent linear model solution.

4. The perturbation energy equation

The behavior of an unstable perturbation growing on some basic-state flow field can be examined by considering the energy equation for the perturbation. For the open-ocean domain considered here, this equation is obtained by multiplying Eq. (18) by $\delta\psi$ and integrating over the entire domain. After integration by parts, neglecting dissipative terms, and application of the perturbation boundary conditions we obtain

$$\int_{-l_x}^{l_x}\int_{-l_y}^{l_y}\int_{-H}^{0}\frac{\partial \mathcal{E}}{\partial t}+\mathbf{V}\cdot\nabla\mathcal{E}\,dxdydz=\int_{-l_x}^{l_x}\int_{-l_y}^{l_y}\int_{-H}^{0}\alpha\Bigg[-V_0\frac{\partial}{\partial x}\left(\frac{\partial\delta\psi}{\partial x}\frac{\partial\delta\psi}{\partial y}\right)-U_0\frac{\partial}{\partial y}\left(\frac{\partial\delta\psi}{\partial x}\frac{\partial\delta\psi}{\partial y}\right)+U_0\frac{\partial}{\partial x}\left(\frac{\partial\delta\psi}{\partial y}\frac{\partial\delta\psi}{\partial y}\right)$$
$$+V_0\frac{\partial}{\partial y}\left(\frac{\partial\delta\psi}{\partial x}\frac{\partial\delta\psi}{\partial x}\right)\Bigg]dxdydz+\int_{-l_x}^{l_x}\int_{-l_y}^{l_y}\int_{-H}^{0}\alpha\Gamma^2\Bigg[-V_0\frac{\partial}{\partial z}\left(\sigma\frac{\partial\delta\psi}{\partial y}\frac{\partial\delta\psi}{\partial z}\right)+U_0\frac{\partial}{\partial z}\left(\sigma\frac{\partial\delta\psi}{\partial x}\frac{\partial\delta\psi}{\partial z}\right)\Bigg]dxdydz, \quad (27)$$

where $\mathbf{V} = U_0\mathbf{i} + V_0\mathbf{j}$, and $U_0 = -\partial\psi/\partial y$ and $V_0 = \partial\psi/\partial x$ are the zonal and meridional components of the basic-state flow field in the direction of the unit vectors $\mathbf{i}$ and $\mathbf{j}$; $\mathcal{E}$ is the perturbation energy given by

$$\mathcal{E}=\frac{1}{2}\left[\left(\frac{\partial\delta\psi}{\partial x}\right)^2+\left(\frac{\partial\delta\psi}{\partial y}\right)^2+\Gamma^2\sigma\left(\frac{\partial\delta\psi}{\partial z}\right)^2\right]. \quad (28)$$

The velocities and density of the perturbation flow are given by

$$u'=-\frac{\partial\delta\psi}{\partial y};\quad v'=\frac{\partial\delta\psi}{\partial x};\quad \theta'=\frac{\partial\delta\psi}{\partial z}. \quad (29)$$

The perturbation energy equation for the model domain can be written more concisely as

$$\int_{-l_x}^{l_x}\int_{-l_y}^{l_y}\int_{-H}^{0}\frac{D\mathcal{E}}{Dt}\,dxdydz=\alpha\int_{-l_x}^{l_x}\int_{-l_y}^{l_y}\int_{-H}^{0}\Bigg[V_0\frac{\partial}{\partial x}(u'v')+U_0\frac{\partial}{\partial y}(u'v')+U_0\frac{\partial}{\partial x}(u'^2)$$
$$+V_0\frac{\partial}{\partial y}(v'^2)\Bigg]dxdydz+\alpha\Gamma^2\int_{-l_x}^{l_x}\int_{-l_y}^{l_y}\int_{-H}^{0}\left[V_0\frac{\partial}{\partial z}(\sigma u'\theta')-U_0\frac{\partial}{\partial z}(\sigma v'\theta')\right]dxdydz, \quad (30)$$

where D/Dt is the "total" rate of change operator following a fluid element.

The first term on the right-hand side of (30) represents the integral of the time rate of change of perturbation energy sources due to barotropic processes. The sum of all terms under the integral represents the rate at which kinetic energy is transferred between the perturbation and the mean flow due to the work done by the Reynolds stresses ($u'v'$, $u'u'$, $v'v'$) on the mean flow. The second term on the right-hand side of (30) represents the integral of the time rate of change of perturbation energy source terms due to baroclinic processes. Each term in this integral represents the rate at which the perturbation density (or heat) fluxes release potential energy from the vertical shear of the basic-state flow field. For brevity, we will refer to the quantity whose integral is the rate of release of perturbation energy by barotropic and baroclinic processes as C_{trop} and C_{clin}. We can, therefore, write Eq. (30) as

$$\int_{-l_x}^{l_x}\int_{-l_y}^{l_y}\int_{-H}^{0}\frac{D\mathcal{E}}{Dt}\,dxdydz=\int_{-l_x}^{l_x}\int_{-l_y}^{l_y}\int_{-H}^{0}C_{\text{trop}}dxdydz+\int_{-l_x}^{l_x}\int_{-l_y}^{l_y}\int_{-H}^{0}C_{\text{clin}}dxdydz. \quad (31)$$

Baroclinic instabilities are associated with the presence of vertical shears in the velocity, which implies the existence of a horizontal temperature gradient. For a basic-state flow possessing only vertical shear, particle motions associated with growing perturbations are, on average, so directed as to produce a thermal flux down the temperature gradient of the basic state so as to release available potential energy. Regions of baroclinic energetics can usually be recognized by the tendency of perturbation streamlines to slope upstream in the vertical plane. The reverse is true in regions of decay in which perturbation streamlines slope downstream in the vertical plane.

Barotropic instabilities arise due to the presence of a horizontal mean-flow strain rate. In this case, particle motions are so directed as to produce a Reynolds stress directed down the basic-state momentum gradients so as to release available kinetic energy. A region of barotropic instability growth can usually be recognized by a tendency for the perturbation streamlines to slope upstream in the horizontal plane.

5. The basic-state flow field

As discussed in the Introduction, the purpose of this study is twofold: (i) we are interested in the stability properties of a given flow field, and (ii) we wish to find the structure and growth of optimal perturbations arising in the field of random perturbations on the initial conditions of a numerical model and so assess the model's predictability.

It remains to choose a basic-state flow field to examine? We could consider the stability of Gulf Stream–like jets in our open-ocean domain. However, this case is similar to the work presented in earlier studies by Orlanski and Cox (1973), Holland and Haidvogel (1980), and Farrell and Moore (1992). Alternatively, we could consider the ensemble average of a number of different kinds of events, such as the formation of warm core and cold core eddies, and try to understand the dynamics of the instability processes underlying these events. Clearly, the latter case would involve a large number of experiments. For this reason, we have chosen to examine the stability of a single observed event. From a modeling viewpoint, the results obtained are applicable to the problem of predictability, and our experiments and analyses emphasize the wealth of information that the method provides about instability mechanisms in general.

The events that we shall examine are the evolution of Gulf Stream meanders and eddies observed during late January and early February in 1988 as part of the Harvard University GULFCAST experiment (Robinson et al. 1989a,b). The model was initialized using a so-called "feature model" approximation to the Gulf Stream based upon AVHRR data, AXBT observations, and Geosat altimeter data collected on or around 27 January 1988 (Robinson et al. 1989a,b). The quasi-geostrophic model was run forward in time for 9 days to predict the ensuing evolution of the Gulf Stream. The model domain used was flat bottomed and rectangular, being 1155 km in length and 720 km wide, centered at 38.3°N, 62.8°E, and rotated 22° anticlockwise to the zonal direction. Full details of the model initialization procedure are given in Robinson and Walstad (1987).

The feature model used to initialize the numerical model is described in detail in Robinson et al. (1988) and is of the following form:

$$\mu=\begin{cases}\exp\left(-\dfrac{y^2}{g_0^2}\right)V_T\left[\left(1-\dfrac{V_M}{V_T}\right)\dfrac{z}{h_s}+1\right], & z>-h_s\\[2ex] \exp\left(-\dfrac{y^2}{g_0^2}\right)V_M\left[\left(1-\dfrac{V_B}{V_M}\right)\dfrac{z}{H-h_s}+1\right], & z<-h_s,\end{cases} \quad (32)$$

where μ is the alongstream velocity component, the across-stream component being identically zero; y is the across-stream coordinate; h_s (=1000 m) is the depth at which $\mu = V_M$ along the stream axis, and H is the depth of the ocean; V_T, V_M, and V_B are the surface, thermocline, and bottom values of velocity along the stream axis taken to be 1.65 m s^{-1}, 0.25 m s^{-1}, and 0.05 m s^{-1}, respectively; and g_0 is the horizontal e-folding length scale of the jet taken to be 40 km. The geographical position and shape of the Gulf Stream axis (i.e. $y = 0$), used in Eq. (32), was determined from AVHRR data.

The basic-state streamfunction ψ at a depth of 150 m on days 5, 7, and 9 of the model integration is shown in Figs. 1a, 1b, and 1c. The dominant feature is the large meander labeled M2, present near the center of the model domain. Over the 4-day period shown, this meander steepens and begins to detach from the main stream and by day 9 has formed a cold core eddy. Another important event to note is the steepening of the meander labeled M1, and the interaction between the warm core eddy W1 with the main stream near the western edge of the model domain. We will examine the stability of the flow regimes depicted in Figs. 1a–1c.

6. Unstable waves on Gulf Stream flows stationary in time

In this section we will consider the stability of Gulf Stream flows, stationary in time as would occur if ap-

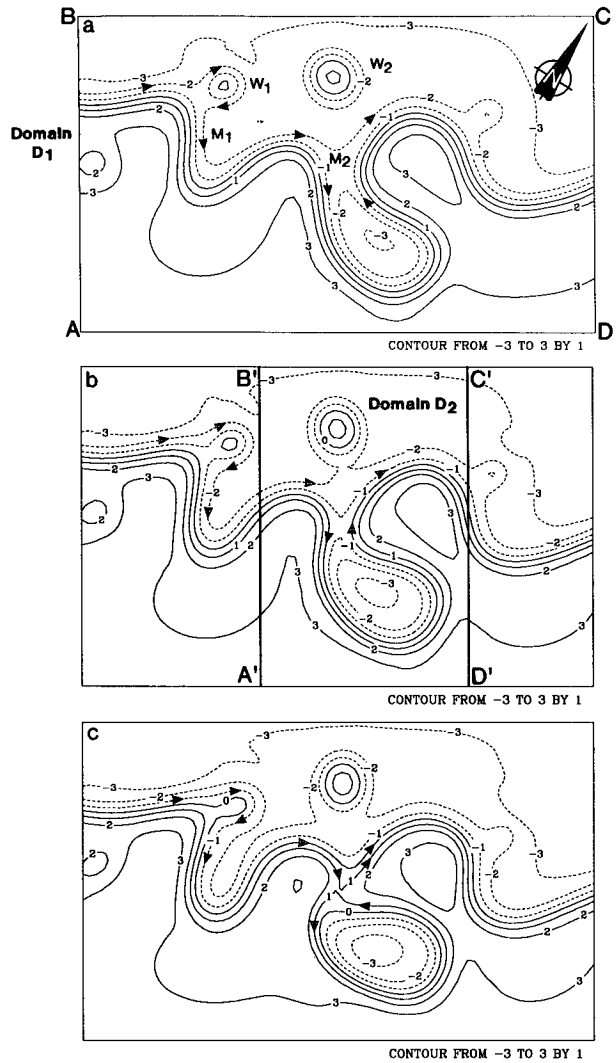

FIG. 1. Basic-state streamfunction ψ at depth 150 m after (a) 5 days, (b) 7 days, (c) 9 days of integration.

propriate forcings were included to balance the mean-flow temporal variation (Pedlosky 1979). Some of the modes and perturbations discussed below are summarized in Table 1.

a. The fastest growing normal mode

The perturbation we shall consider first is the fastest-growing normal mode. As discussed in section 2, one advantage of considering perturbations of modal form is that they grow at the same exponential rate in all norms. The fastest-growing normal mode was found by integrating the tangent linear equation (18) for $\delta\psi$ forward in time starting from an arbitrary nonzero initial condition in the form of random noise. The fastest-growing normal mode eventually dominated the model solution. As with all forms of linear, stability analysis, the mode so generated has arbitrary phase and amplitude.

Figure 2 shows $\delta\psi$ at 150 m for the fastest-growing normal mode (hereafter referred to as FGNM) on the Gulf Stream flow of Fig. 1a, which was assumed rendered stationary in time. The approximate position of the Gulf Stream axis on this day is also indicated. The alongstream wavelength varies between 250 km and 500 km, and the period of the mode is close to 31 days. Three phases of the mode 8 days apart (approximately 1/4 wave period) are shown in Fig. 2.

The time-averaged energetics of FGNM were examined by suppressing the exponential growth factor of the mode and averaging over a wave period. This approach is equivalent to the "random phase ensemble mean" analyses of Frederiksen (1982). The random phase ensemble mean total perturbation energy of FGNM at a depth of 150 m is shown in Fig. 3a. The perturbation energy is localized, particularly in the southward-flowing arm of the meander M2 and downstream of the northward flowing arm. The region in which the warm core eddy W1 interacts with the main stream is also a region of significant energy release. Perhaps the most dominant feature in Fig. 3a is the region of large perturbation energy associated with warm core eddy W2.

We have used the energy equation (30) to examine the contribution of barotropic and baroclinic processes to the total perturbation energy of FGNM. The kernel of the first term on the right-hand side of (30) represents the rate of release of perturbation energy due to barotropic processes, C_{trop} in (31). Similarly, the kernel of the second term on the right of Eq. (30) represents the rate of release of perturbation energy by baroclinic processes, C_{clin}. Because Eq. (30) has been obtained through integration by parts, C_{trop} and C_{clin} can only be interpreted in an integral sense and so are indicative of the physical processes occuring over a region rather than at a point. The random phase ensemble means of C_{trop} and C_{clin} (hereafter, $\overline{C_{\text{trop}}}$ and $\overline{C_{\text{clin}}}$) are shown in Figs. 3b and 3c, at a depth of 150 m for FGNM. An obvious feature of Figs. 3a and 3b is that there are regions of both energy growth and energy decay. The integral of $\overline{C_{\text{trop}}}$ and $\overline{C_{\text{clin}}}$ over the horizontal domain at 150 m reveals that the average rate of change of perturbation energy due to barotropic and baroclinic processes is positive. This is confirmed in Fig. 4, which

TABLE 1. A summary of some of the modes and perturbations referred to in this study and calculated under the assumption of a Gulf Stream flow that is stationary in time.

Perturbation	Norm growth rate maximized	Period of optimal growth (days)
FGNM	Principal normal mode	—
FGEI	$\delta E = \frac{1}{2}\langle \delta\psi, \delta\psi \rangle$	1
ADNM	Principal adjoint normal mode	—

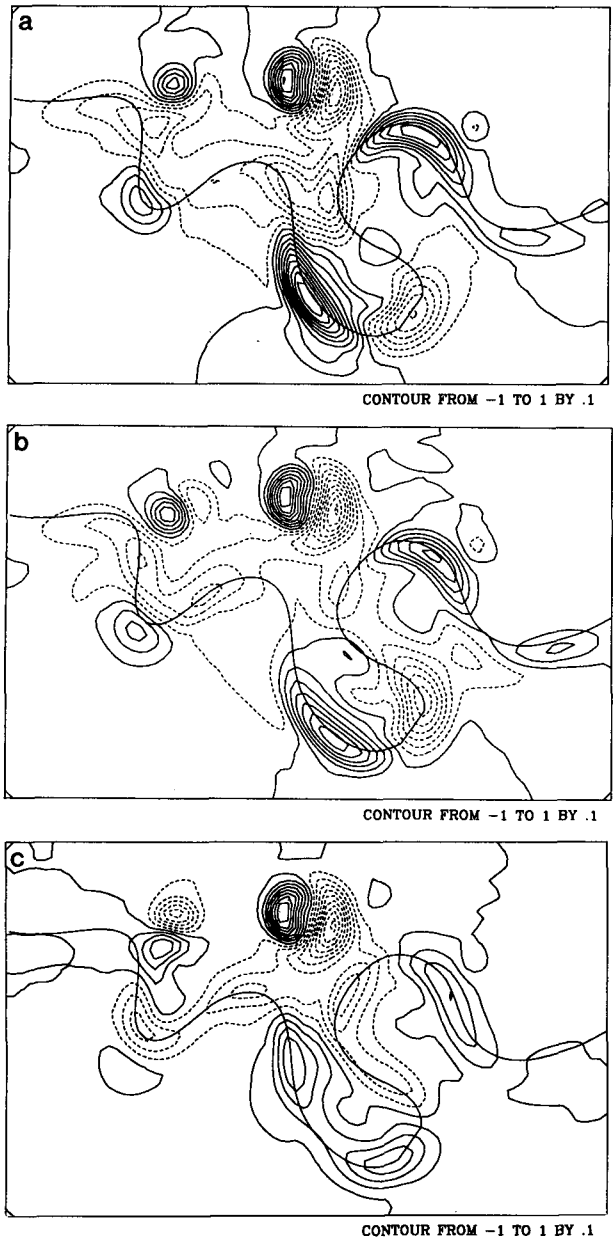

FIG. 2. Perturbation streamfunction $\delta\psi$ for the fastest-growing normal mode, FGNM, on the Gulf Stream flow of Fig. 1a, which was assumed stationary in time. Different phases of the mode are shown 8 days apart. The approximate position of the Gulf Stream axis, taken to be the zero streamline of Fig. 1a, is also drawn.

shows that the total perturbation energy δE for FGNM increases with time. The domain integral of $\overline{C_{\text{trop}}}$ is almost five times larger than the integral of $\overline{C_{\text{clin}}}$, which indicates that the growth of FGNM is dominated by barotropic processes. In agreement with Fig. 3a, the regions of preferred energy release due to barotropic and baroclinic processes are the southward-flowing arm of the meander M2 and downstream of the northward-flowing arm close to the meander neck region. The energy release associated with the interaction of W1 with the main stream is associated primarily with barotropic instability, while the energetic warm core eddy W2 appears to be influenced almost equally by both barotropic and baroclinic instability. It would appear from $\overline{C_{\text{trop}}}$ and $\overline{C_{\text{clin}}}$ that the basic-state flow of Fig. 1a is unstable with respect to both barotropic and baroclinic processes.

It is illuminating to examine the instantaneous rate of change of the perturbation energy associated with a particular configuration of $\delta\psi$, since this reveals the

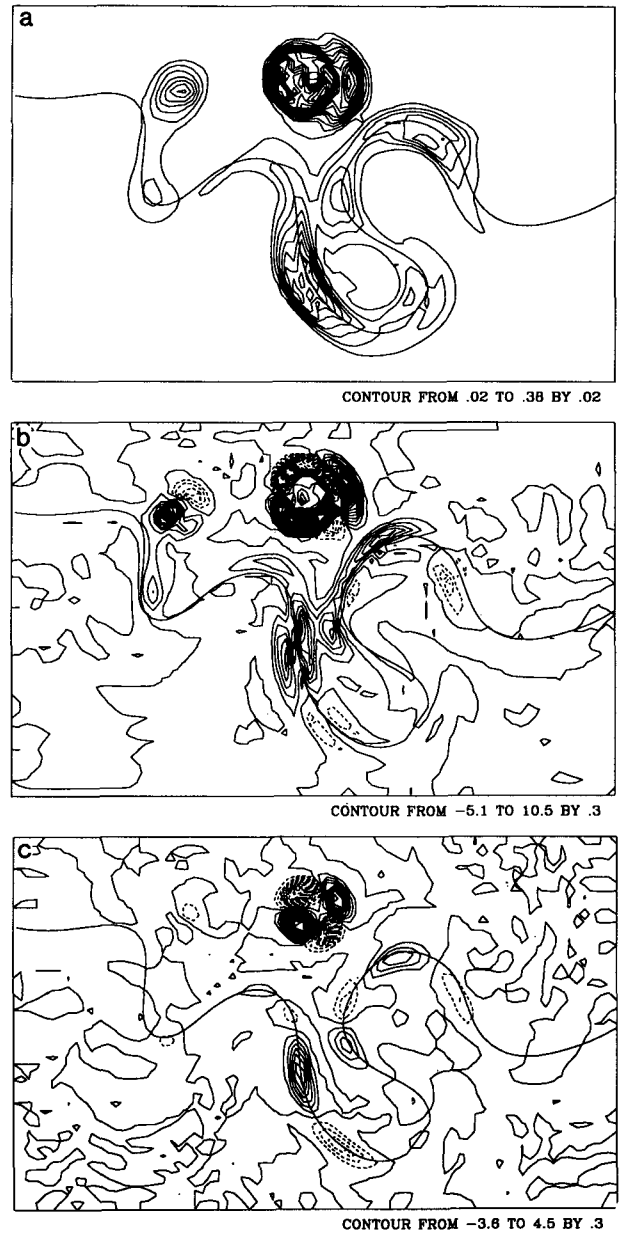

FIG. 3. Random phase ensemble means of (a) perturbation energy $\mathcal{E}$, (b) C_{trop}, and (c) C_{clin}, for FGNM.

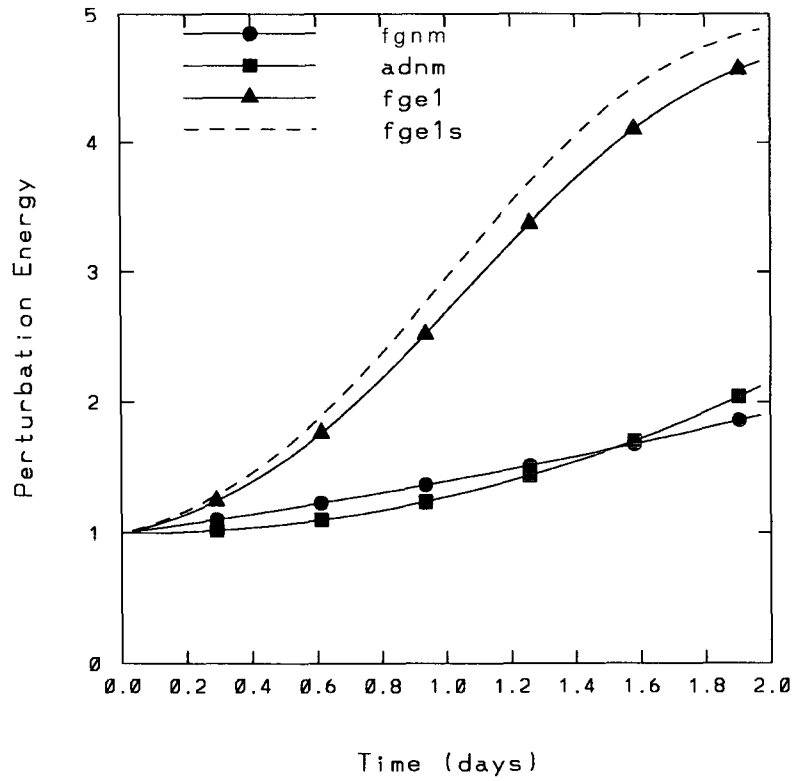

FIG. 4. Time evolution of δE for different normal modes and optimal perturbation.

way in which basic-state energy is transferred to the perturbation. Figures 5a and 5b show, respectively, snapshots of the barotropic energy kernel C_{trop} and the baroclinic energy kernel C_{clin} at 150 m during the phase of FGNM shown in Fig. 2a. Energy growth due to barotropic processes can be seen to occur in regions where perturbation streamlines $\delta\psi$ slope upstream in the horizontal plane and release available KE. Conversely, barotropic processes lead to decay in regions where $\delta\psi$ slopes downstream and where perturbation energy is converted into basic-state KE.

Figure 6 shows a snapshot vertical section of $\delta\psi$ from Fig. 2a taken along the axis of the Gulf Stream. Energy growth due to baroclinic processes (Fig. 5b) occurs in regions where the streamlines $\delta\psi$ slope upstream in the vertical plane (as at locations 3 and 6) where available PE is released from the basic-state flow. Conversely, where phase lines of $\delta\psi$ slope downstream (as at location 4 in Fig. 6), C_{clin}, decays as perturbation energy is converted into basic-state PE.

Some aspects of the large-scale evolution of the basic state depicted in Fig. 1 can be explained in terms of the fastest-growing normal mode FGNM. Figure 7 shows the difference $\Delta\psi$ in the basic-state streamfunction ψ between day 5 and day 9 (cf. Fig. 1a minus Fig. 1c). A comparison of Fig. 7 and Fig. 2a shows that apart from a difference in amplitude and phase, FGNM and $\Delta\psi$ share a number of common features. This similarity suggests that FGNM may be an approximate mode of the nonlinear equations (14) and (15) as well as a mode of the tangent linear equation (18). Figure 7, however, suggests that other disturbances also contribute to the large-scale evolution of the basic state.

b. *Optimal perturbations for δE*

Using the iterative method described in section 3, we can find the eigenvector with the largest growth in the perturbation energy norm $\delta E = \frac{1}{2}\langle\delta\psi, \delta\psi\rangle$. The resulting perturbations are referred to as optimal perturbations.

We will show first how the structure of an optimal perturbation changes as the specified time interval of optimal growth is increased. Figure 8 shows $\delta\psi$ at a depth of 150 m at initial time $t = 0$ for optimals that maximize the growth of δE on the flow field of Fig. 1a (assumed rendered stationary in time) over 3 hours (Fig. 8a), 12 hours (Fig. 8b), and 1 day (Fig. 8c). The resulting optimal perturbations will be referred to as FGEE, FGEH, and FGE1, respectively. The number of iterations employed to find each optimal was 800, 200, and 100, respectively, after which no further changes occured in the overall shape and location of each perturbation. As Fig. 8 indicates, the structure of each perturbation changes as the time interval allowed for optimal growth increases, but the region always fa-

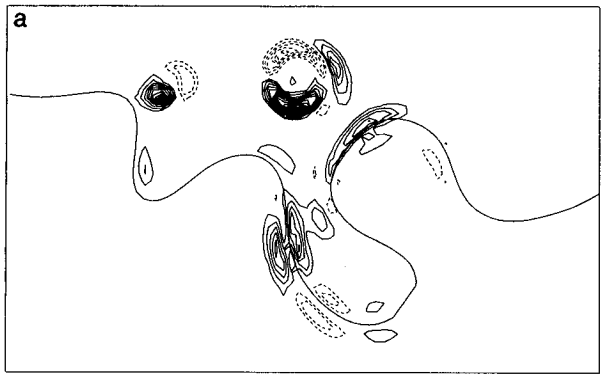

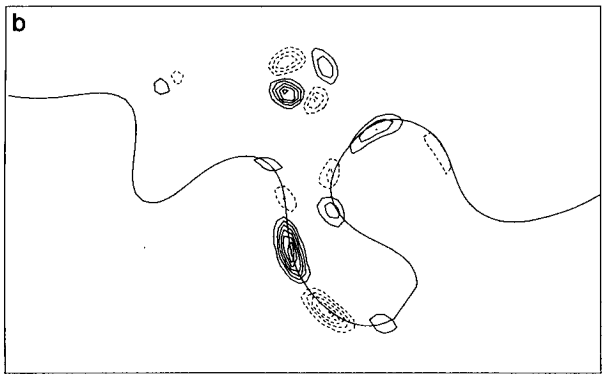

FIG. 5. A snapshot of (a) C_{trop} and (b) C_{clin} at 150 m for FGNM. The zero contour is suppressed for clarity.

vored for growth by the optimal perturbation is the neck of the meander M2. The alongstream wavelength of each optimal shown in Fig. 8 is much less than that of FGNM discussed above. For the remainder of this section, we mainly confine our attention to the optimal referred to as FGE1, which maximizes the growth rate of δE over a 1-day time interval.

The optimal perturbation FGE1 is not of modal form, and so we cannot define a random phase-ensemble mean to study its energetics as we did for FGNM. We will, therefore, restrict our attention to instantaneous energetics using the energy equation (30), noting as before that the various terms in (30) give the contribution to the time rate of change of δE. As such, Eq. (30) indicates the energetic processes that are occuring in a given region rather than at individual points. Figures 9a and 9b show snapshots of the energy kernels C_{trop} and C_{clin}, respectively, for the optimal FGE1 at a depth of 150 m at initial time $t = 0$. In contrast to FGNM of Fig. 2, C_{trop} and C_{clin} for FGE1 are everywhere positive, and regions of maximum growth are concentrated on the southward-flowing and northward-flowing arms that form the neck of meander M2. Comparison of Fig. 9a with Fig. 8c reveals that the regions of maximum C_{trop} occur where phase lines of $\delta\psi$ tilt upstream in the horizontal plane. The neck of M2 is a region of large horizontal velocity shear due to the proximity of the opposing arms of the meander. As a consequence, there is a source of available KE for perturbation growth in this region. As Fig. 9a shows, the region of energy release due to barotropic processes spans the entire neck of M2. In contrast, Fig. 9b shows that C_{clin} is confined mainly to the axis of the Gulf Stream jet. Baroclinic energetics feed on the available PE of the basic-state flow, and it is along the jet axis that the basic-state vertical shears are largest. Figure 10a shows a vertical section of $\delta\psi$ at $t = 0$ for FGE1 taken along the southward-flowing arm of meander M2. The regions of intense baroclinic interaction are clearly associated with regions where the perturbation streamlines slope upstream in the vertical plane. Figures 9a and 9b indicate that at time $t = 0$, the contribution of C_{trop} to the total time rate of change of perturbation energy is larger than the contribution to C_{clin}.

The structure of FGE1 after day 1 is displayed in Fig. 8d, which shows $\delta\psi$ at 150-m depth. The "arrowhead" appearance of $\delta\psi$ in Fig. 8c at $t = 0$ is less pronounced at $t = 1$ day, these structures having evolved into more elliptical features; C_{trop} and C_{clin} of FGE1 at $t = 1$ day are shown in Fig. 11. The general features of the energy growth patterns are similar to those at $t = 0$, only now there are small regions of energy decay where perturbation streamlines slope downstream in the horizontal and vertical planes.

The change in the overall appearance of the optimal FGE1 is consistent with the release of energy from the basic state. In the horizontal plane, the perturbation streamlines advance downstream as time increases, releasing the maximum amount of available KE possible from the basic-state flow in the time available. Figure 10b shows a vertical section of $\delta\psi$ for FGE1 along the axis of the southward-flowing arm of the meander at time $t = 1$ day. As time increases, Fig. 10 reveals that streamlines advance downstream in the vertical plane, releasing the maximum amount of available PE from the basic state in the time available. At time $t = 0$, C_{trop} is larger than C_{clin}, but by time $t = 1$ day, they are similar. It appears, therefore, that FGE1 is able to sustain a rapid growth over the chosen time interval by initially drawing mainly upon the available KE of the basic state through barotropic instability.

To illustrate that FGE1 is indeed optimal in the sense that it maximizes the growth of total perturbation energy δE over a 1-day period, Fig. 4 shows δE for FGE1 as a function of time. Clearly the growth rate of δE during FGE1 exceeds that of the fastest growing mode, FGNM.

As the period of optimal growth τ increases from 3 hours to 1 day, Fig. 8 shows that the horizontal upstream tilt of $\delta\psi$ also increases, which indicates that the amount of available basic-state KE released by each optimal perturbation increases with τ. In a similar way,

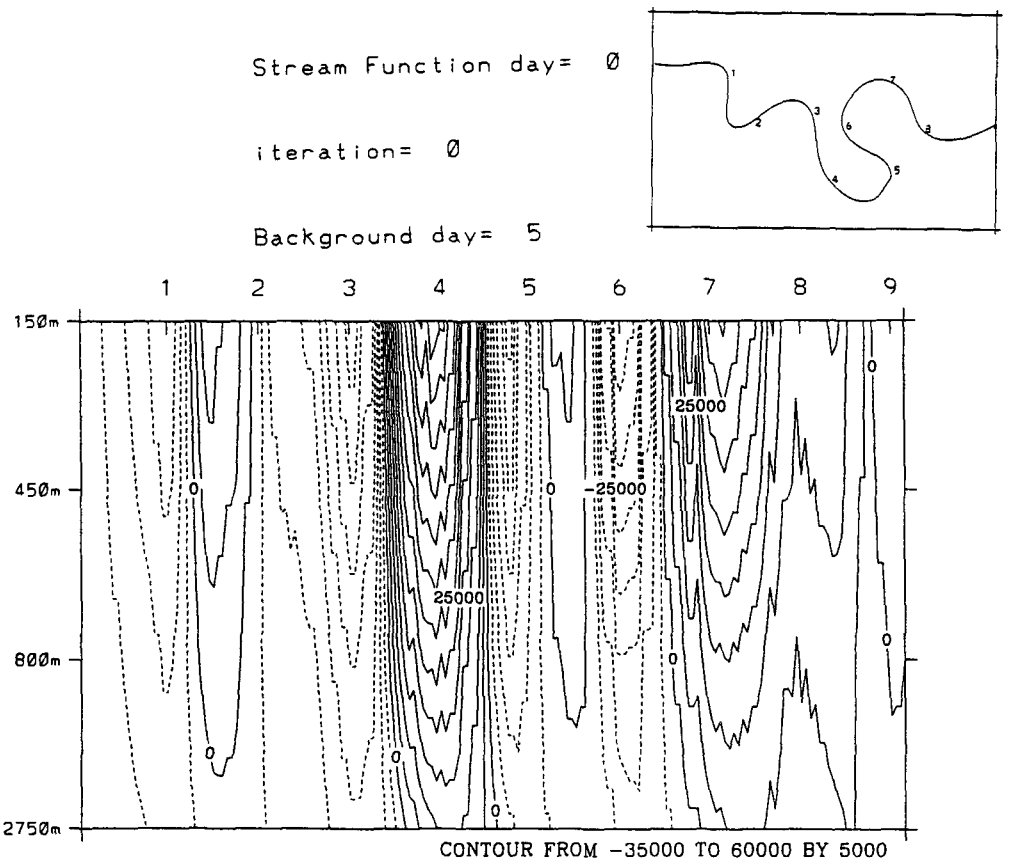

FIG. 6. A vertical cross section of $\delta\psi$ for FGNM along the axis of the Gulf Stream.

an increase in τ is accompanied by an increase in the vertical upstream tilt of $\delta\psi$ and an increase in the release of available basic-state PE. Table 2 presents a summary of the properties of different optimal perturbations for the energy norm and shows that the growth factor λ increases with τ. Also shown in Table 2 is the ratio λ/τ, which is the average time rate of change of λ; λ/τ can be thought of as a measure of a perturbations potential for releasing basic-state energy. Table 2 shows that even though longer τ yields a greater release of basic-state energy, the potential of the perturbation to release energy is diminished. This is also reflected in the peak *e*-folding times attained by each disturbance shown in Table 2; as τ increases, the maximum exponential growth rate attained by each disturbance decreases.

Since we are modeling oceanic flows in an open-ocean domain, it is important to examine the influence of the open boundaries. To investigate the effect that the open boundaries have on the optimal FGE1, we constructed a new model domain (referred to as D_2) that was smaller than the original model domain (referred to as D_1) shown in Fig. 1a. Here D_2 was formed by moving the eastern and western open boundaries, denoted AB and CD in Fig. 1a, to the new locations A'B' and C'D' (shown in Fig. 1b), which are towards the center of D_1. The optimal perturbation for the energy norm over 1 day (hereafter FGE1s) was then computed for the Gulf Stream flow field bounded by A'B'C'D' of D_2. The boundary conditions imposed on the tangent linear and adjoint models along A'B', B'C',

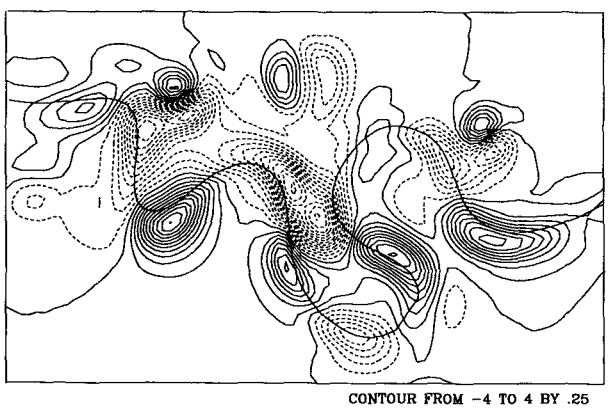

FIG. 7. The difference in ψ of the basic state between day 5 (Fig. 1a) and day 7 (Fig. 1b).

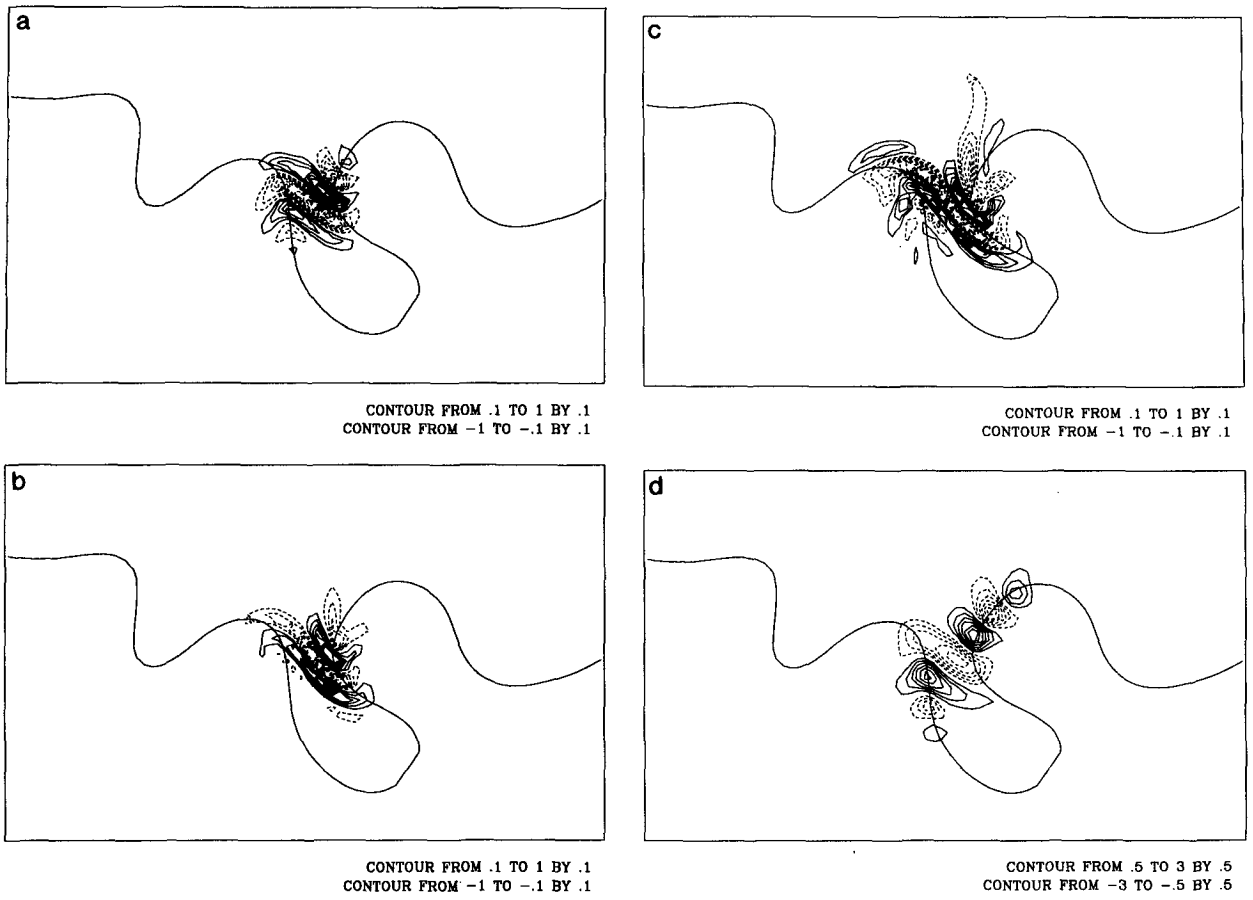

FIG. 8. $\delta\psi$ at 150 m and $t = 0$ for the optimal perturbations that maximize the growth rate of δE over (a) 3 hours, FGEE; (b) 12 hours, FGEH; (c) 1 day, FGE1, on the stationary basic state of Fig. 1a; and (d) as in (c) but at time $t = 1$ day.

C'D', and D'A' of D_2 were identical to those described in section 3.

Figure 12 shows $\delta\psi$ at 150 m and $t = 0$ for FGE1s, and a comparison with Fig. 8c shows that FGE1s is almost identical to the energy optimal FGE1 of D_1. The growth of δE for FGE1s is shown in Fig. 4 and is very similar to that of FGE1. Clearly the structure and location of the optimal perturbation in this case is insensitive to the location of the open boundaries.

c. *Optimal excitations for the normal mode*

The biorthogonality relation (11) for normal modes of the tangent linear and adjoint equations can be used to find the optimal excitations for a given mode. Because the system is not self-adjoint, the normal modes are not orthogonal, and a given mode will not be its own optimal excitation. Before we can find the optimal excitation for a given mode, we must first decide in what sense it is to be considered optimal.

It can easily be shown from Eqs. (11) and (13) that the optimal excitation for the fastest-growing normal mode of Eqs. (18) and (19) (Fig. 2) in the energy norm δE is the fastest-growing normal mode of the adjoint equation (22). As in the case of the mode FGNM, the fastest-growing adjoint normal mode (hereafter referred to as ADNM) can be found by integrating Eq. (22) starting from random noise until the fastest-growing adjoint normal mode dominates the solution. Figure 13 shows a snapshot of $\delta\psi^*$ at 150 m for ADNM obtained in this way. The growth rate of δE following the initialization of the tangent linear model with ADNM is shown in Fig. 4. Figure 4 shows that the growth rate of ADNM eventually overtakes that of FGNM. Clearly, however, the optimal excitation for FGNM grows much less rapidly in energy than the optimal perturbation FGE1.

7. Unstable waves on time-varying Gulf Stream flows

In this section we will examine the effect that a time-varying Gulf Stream flow has on the optimal perturbations and normal modes. We will limit our attention to optimals that maximize the growth rate of δE. The time-varying Gulf Stream flow considered here is the

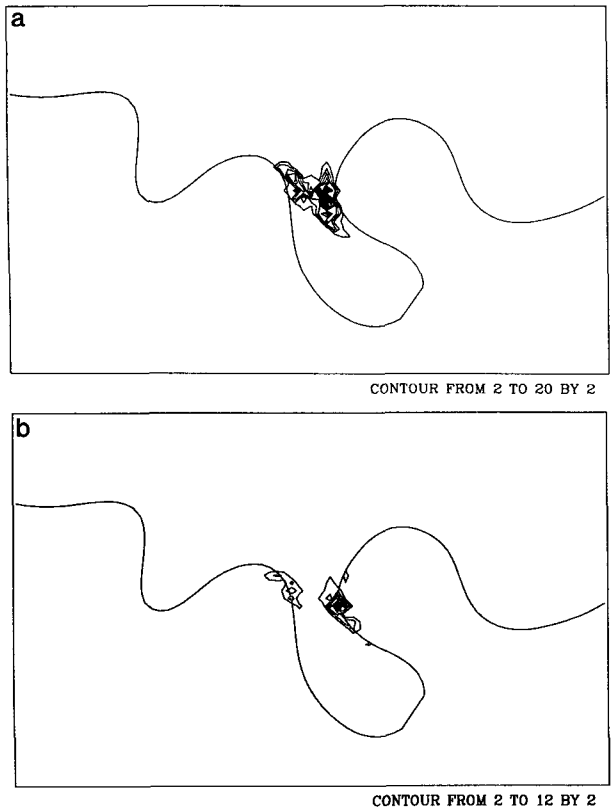

FIG. 9. (a) C_{trop} and (b) C_{clin} at 150 m and $t = 0$ for FGE1. The zero contour is suppressed for clarity.

4-day period depicted in Figs. 1a, 1b, and 1c, during which the large meander M2 steepens and detaches from the main stream to form a cold core eddy. Other events to note are the steepening of the meander labeled M1 located close to the inflow at the western boundary and the strong interaction that occurs between warm core ring W1 and the main Gulf Stream.

Optimal perturbations on time-varying Gulf Stream flows were found using the iterative method described in section 3, with ψ of Eqs. (18) and (22) varying in time. Figure 14 shows $\delta\psi$ at $t = 0$ for optimal perturbations that maximize the growth of δE over time intervals of 2 days, 3 days, 3 1/2 days, and 4 days, where time $t = 0$ corresponds to the Gulf Stream flow of Fig. 1a. Figures 14a and 14b show that the preferred region of growth is the neck of meander M2, and as the time period of optimal growth increases from 2 to 3 days, the tilt of the streamlines upstream in the horizontal plane increases. When the period of optimal growth reaches 3 1/2 days (Fig. 14c), other regions of growth are favored by the perturbation. In addition to the neck of M2, Fig. 14c shows that the region where W1 merges with the main stream is also favored for growth by the optimal. When the period for optimal growth is increased to 4 days (Fig. 14d), the neck of M2 is no longer favored for energy growth by the optimal. Instead, the energy optimal perturbation is localized entirely in the region where W1 merges with the Gulf Stream.

To illustrate that the behavior of the optimal is governed by the time history of the Gulf Stream flow, Figs. 15a and 15b show $\delta\psi$ at $t = 0$ for optimal perturbations that grow most rapidly in δE over 2 days and 4 days, respectively, on the Gulf Stream flow of Fig. 1a, assumed rendered stationary in time. As the time period for optimal growth increases, the area occupied by the perturbation becomes larger, but in both cases the neck of M2 is favored for growth.

Our results show that the neck of M2 acts as a source of energy for the optimal perturbations considered. However, for time-varying flows, meander M2 becomes less favorable for growth over longer time intervals because as Fig. 1 shows, M2 gradually steepens and forms a cold core eddy. Once this eddy detaches from the main Gulf Stream, the neck of M2 disappears and along with it the region of large shear and large rate of strain. Perturbations forming in the neck of M2 at times before this (cf. Figs. 1a and 1b) will therefore have a limited source of energy with which to grow after detachment of M2 has occurred. The energy source associated with M2 disappears when the eddy forms, and this will most likely lead to the decay of perturbations that form in the neck of M2 because they will be unable to sustain rapid growth for the full 4-day period depicted in Fig. 1. In order to be optimal, the perturbations will instead seek alternative sites for growth, and as Fig. 14d shows, a suitable location is the region where W1 merges with the Gulf Stream.

To further illustrate the important influence that a time-varying flow has on the preferred location of the energy optimal, Figs. 16a and 16b show optimals that maximize the growth of δE over 1 day on the Gulf Stream flows of Figs. 1b and 1c, respectively, if it is assumed that these flows are rendered stationary in time. In Fig. 16a, M2 is still attached to the main Gulf Stream and the energy optimal favors the neck of M2 for growth. In Fig. 16b, however, M2 has evolved into an eddy, and it is this eddy that is favored by the perturbation for optimal growth. Figure 16c shows the energy optimal for a 2-day time interval that spans the period when M2 separates from the Gulf Stream. In this case a time-varying Gulf Stream flow is used to calculate the optimal so that the perturbation knows about the formation of the eddy. In appearance, the resulting optimal of Fig. 16c looks like a combination of the optimals depicted in Figs. 16a and 16b. As time advances, the optimal of Fig. 16c develops both on the southward-flowing arm of the cold core eddy and on the main axis of the Gulf Stream.

This demonstrates that the formation of the cold core eddy is not sufficient to preclude the growth of optimal disturbances in the region of M2. It would appear that the actual time history of the basic state also plays an important role in determining the preferred location of optimal growth. This idea is con-

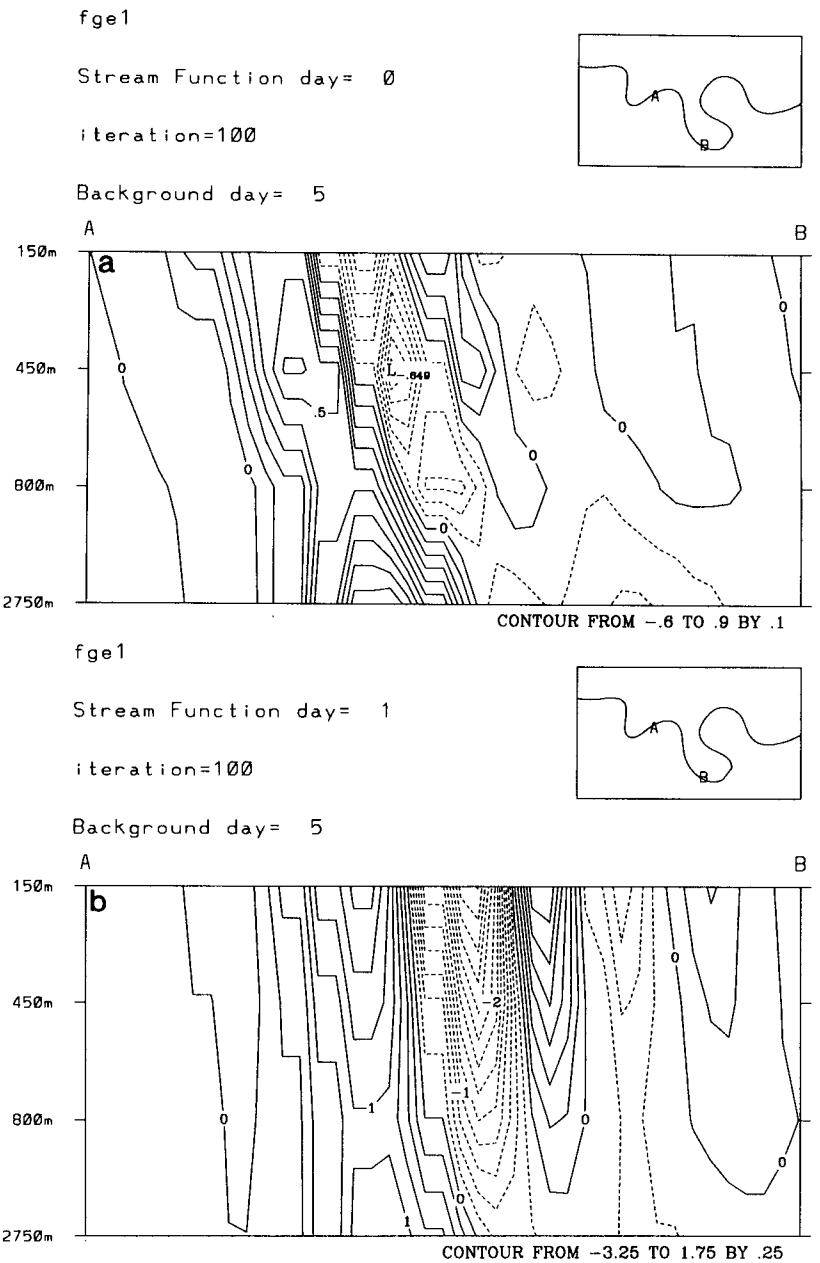

FIG. 10. A vertical cross section of $\delta\psi$ for FGE1 at (a) $t = 0$, (b) $t = 1$ day.

firmed if we note that for each optimal in Fig. 8, at no time is the region of eddy–mean flow interaction associated with W1 a preferred region of growth, as was the case for the optimal perturbations of Figs. 14c and 14d that develop on time-evolving basic states. Table 2 compares the growth factors λ of optimal perturbations for stationary and time-evolving basic states. In general, Table 2 shows that optimal perturbations for time-evolving flows tend to grow faster than their counterparts on flows assumed stationary in time.

The normal modes of the system are also influenced by a time-varying Gulf Stream. The normal modes in this case were found by employing the iterative technique described previously, which has also been used recently by Joly and Thorpe (1991) for time-varying flows, to examine the normal modes associated with frontogenesis in the atmosphere. The tangent linear model is integrated forward in time over an interval τ starting from a random noise field, but in this case ψ of Eq. (18) varies with time as in Fig. 1. At the end of each iteration, the $\delta\psi$ field so obtained becomes the initial condition for the next iteration. The fastest-

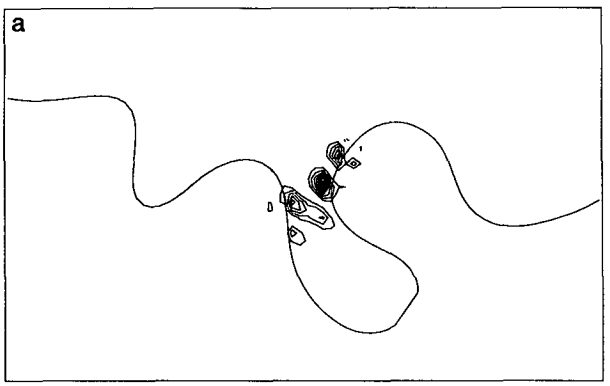

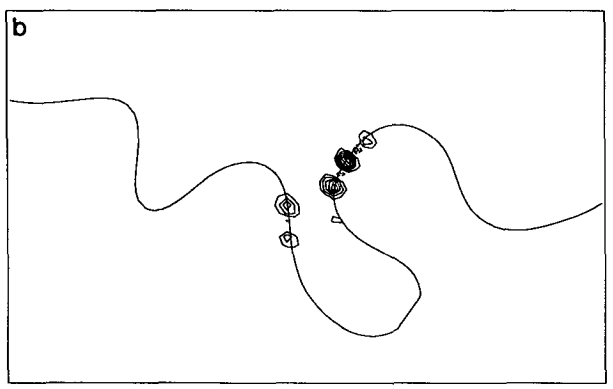

FIG. 11. (a) C_{trop} and (b) C_{clin} at 150 m and $t = 1$ day for FGE1. The zero contour is suppressed for clarity.

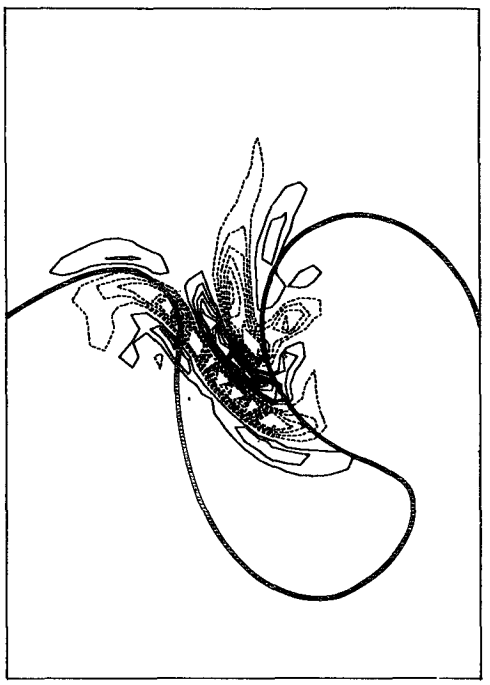

FIG. 12. $\delta\psi$ at 150 m and $t = 0$ for FGE1S, the optimal perturbation that maximizes perturbation energy growth over day in domain D_2.

growing normal mode associated with the time-dependent basic state eventually dominates the tangent linear solution.

Two normal modes were computed for Gulf Stream flows varying in time over 2 days and 4 days, with the flow field of Fig. 1a defining initial time $t = 0$ in each

TABLE 2. A summary of the growth $\lambda = \delta E(\tau)/\delta E(0)$, period of optimal growth τ, and e-folding times attained by the different optimal perturbations and principle normal modes considered in this study. The basic state is referred to as stationary (S) or time dependent (T), and for stationary states the Gulf Stream flow used is indicated by a figure reference.

Perturbation description	λ	τ (days)	λ/τ $(\text{days})^{-1}$	Peak e-folding time of δE (days)	Basic state
Principle mode (*FGNM*)	1.39	1		2.94	S (Fig 1a)
Energy optimal	1.2	1/8	9.6	0.60	S (Fig 1a)
Energy optimal	2.0	1/2	4.0	0.63	S (Fig 1a)
Energy optimal (*FGE1*)	4.0	1	4.0	0.62	S (Fig 1a)
Energy optimal	11.5	2	5.8	0.67	S (Fig 1a)
Energy optimal	30.3	3	10.1	0.71	S (Fig 1a)
Energy optimal	66.7	4	16.7	0.75	S (Fig 1a)
Energy optimal	4.2	1	4.2	0.61	T
Energy optimal	12.9	2	6.45	0.63	T
Energy optimal	32.2	3	10.7	0.67	T
Energy optimal	77.1	4	19.3	0.68	T
Principle mode	2.21	2		2.40	T
Principle mode	2.88	3		2.61	T
Principle mode	4.26	4		2.41	T

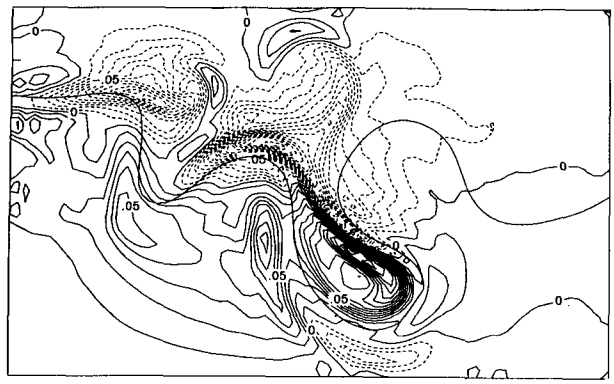

FIG. 13. $\delta\psi$ at 150 m for the fastest-growing normal mode ADNM of the adjoint model.

case. Figure 17 shows $\delta\psi$ at the initial time for each mode. As the time over which the Gulf Stream evolves is increased from 2 days (Fig. 17a) to 4 days (Fig. 17b), the region influenced by the growth of the principle normal mode decreases.

8. Concluding remarks

The optimal perturbations that we have found in this study tell us where and how perturbations to a Gulf Stream basic-state flow can achieve maximum growth in the perturbation energy norm over a given time interval. Studies of optimal perturbations are important because they reveal the mechanisms by which disturbances can achieve rapid growth and the locations in which rapid growth can occur. Using this knowledge, suboptimal perturbations with structures similar to but less specialized than optimal perturbations can be constructed, which nevertheless grow more rapidly than normal modes as demonstrated by Farrell (1985). Suboptimal disturbances must arise in models as a result of uncertainties in the model initial conditions due to observation errors or analysis errors, since every error projects onto the complete optimal set that includes this most rapidly growing member. Further-

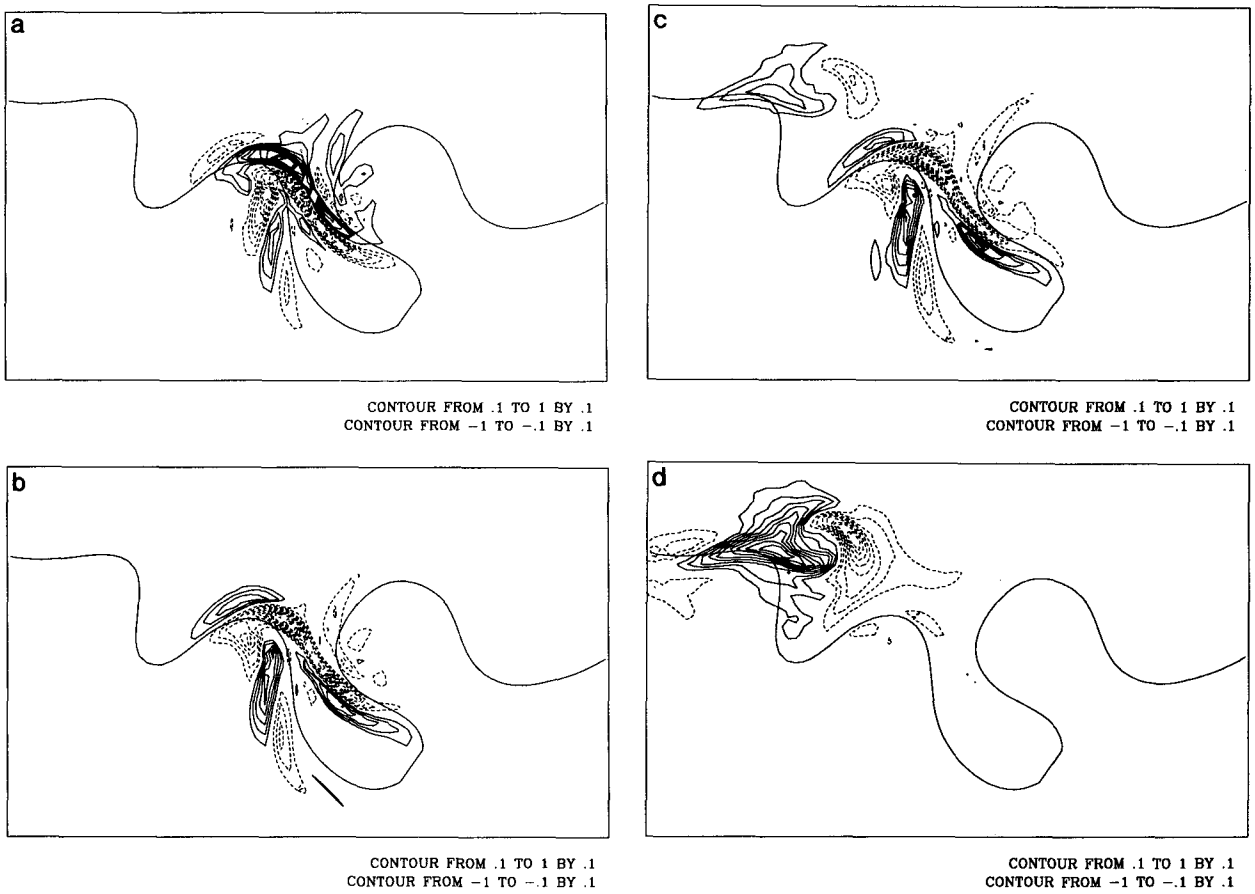

FIG. 14. $\delta\psi$ at 150 m and $t = 0$ for optimal perturbations that maximize the growth of δE over time intervals of (a) 2 days, (b) 3 days, (c) 3½ days, (d) 4 days on a time-varying Gulf Stream flow.

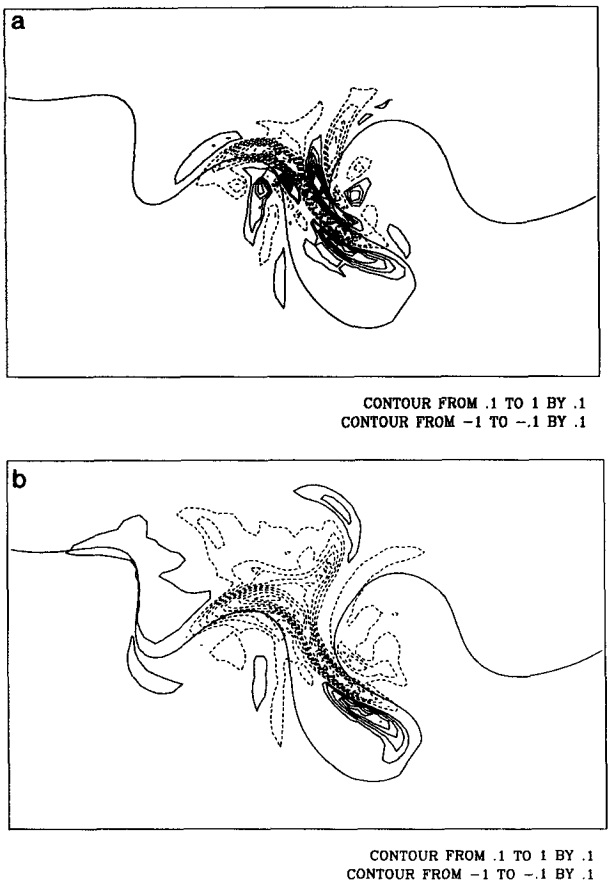

FIG. 15. $\delta\psi$ at 150 m and $t = 0$ for optimal perturbations that maximize the growth of δE over time intervals of (a) 2 days and (b) 4 days on the Gulf Stream flow of Fig. 1a when assumed stationary in time.

more, parameterizations of physical processes such as convection could introduce highly structured small-scale errors into models if, for example, convection was to occur in the model at the wrong location or at the incorrect time. The rapid development of such small-scale optimals may be related to the observation of Lorenz (1969a) that small-scale model errors amplify more rapidly than errors on the large scale. Clearly, the results and ideas presented here are relevant to the question of the predictability of oceanic flows such as those of Fig. 1, since uncertainties in the model initial conditions may amplify in the unstable regions, suggested by the optimal perturbations.

The dynamics of an error in the initial conditions of a model can be viewed as the evolution along the solution trajectory of the initial error (Lorenz 1965; Farrell 1990). Following this argument further, let us assume that the initial errors of the system are spherically distributed in some norm, say energy. As the system evolves in time, the sphere becomes an ellipsoid, the semiaxes of which are proportional to the square root of the eigenvalues of the matrix $\mathbf{R}_\tau^*\mathbf{R}_\tau$ in Eq. (10). The eigenvector of this matrix associated with the largest eigenvalue is the one that grows the most over the time interval τ in the chosen norm. To completely un-

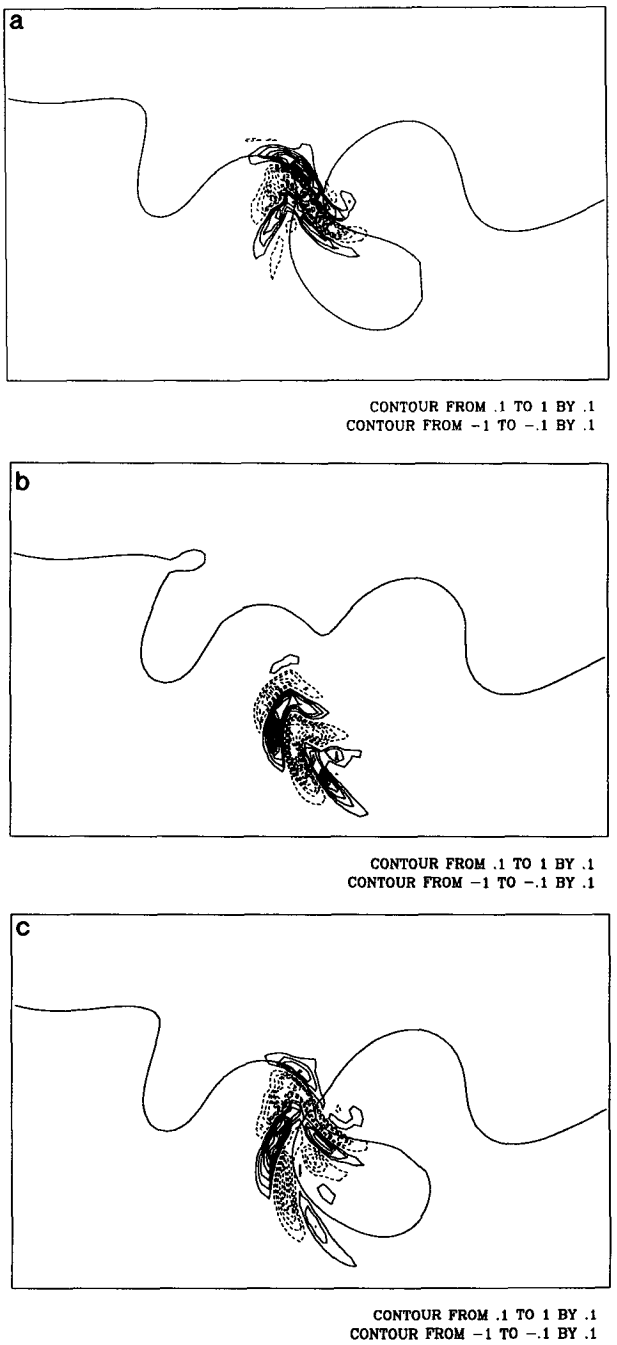

FIG. 16. $\delta\psi$ at 150 m and $t = 0$ for optimal perturbations that maximize the growth of δE (a) over 1 day on the Gulf Stream flow of Fig. 1b when assumed stationary in time, (b) as (a) but for the flow of Fig. 1c, and (c) over 2 days on a time-varying Gulf Stream flow during the period when meander M2 detaches from the main stream.

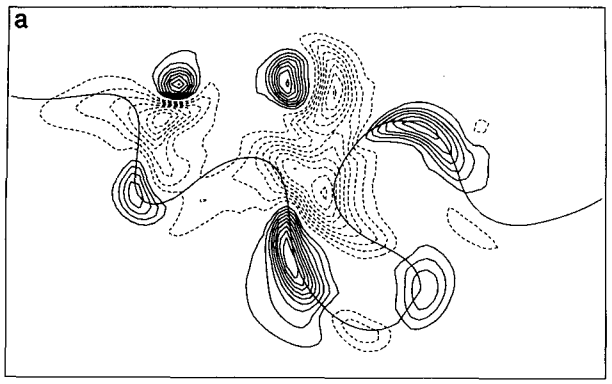

FIG. 17. $\delta\psi$ at depth 150 m for the fastest-growing normal mode on the Gulf Stream varying in time over (a) 2 days and (b) 4 days.

derstand the predictability of a given flow field, we require the complete spectrum of eigenvalues λ_i, since perturbation variance is dependent upon the entire spectrum. The values of $\lambda_i > 1$ are associated with perturbations that grow in time in the chosen norm, while those with $\lambda_i < 1$ decay. Farrell (1990) has considered the predictability of several simplified flow fields of relevance to the oceanic and atmospheric circulations, and in general, finds that only a few percent of the eigenfunctions of the perturbation energy matrix have significant growth rates. In other words, the predictability of the flow may be determined by only the first few optimal perturbations.

To determine the predictability of flows such as that of Fig. 1, we need to examine the behavior of other eigenfunctions of the optimal problems considered and not confine our attention to the fastest growing. This is probably impractical using the iterative method employed here, but more eigenfunctions could be found using currently available eigenanalysis routines, even for systems as large as that considered here. This will be the subject of a subsequent paper.

Even though we have found only the first member of the entire spectrum of eigenfunctions, it is still interesting to speculate how the predictability of the system might be influenced by the fastest-growing eigenvectors found for the energy norm. Table 2 shows the peak e-folding time of $\delta E = \frac{1}{2}\langle \delta\psi, \delta\psi \rangle$ achieved by each of the fastest-growing normal modes and optimal perturbations considered in sections 6 and 7. For the case with a stationary basic state, the optimal perturbation FGE1 over 1 day grows almost five times faster than the fastest-growing mode FGNM. Increasing the time interval of optimal growth from 1 to 4 days reduces the growth rate of FGE1 by a factor of 1.2, but even so, the 4-day energy optimal still grows four times faster than FGNM. We have found that the time history of the basic-state flow can significantly influence the growth rate and preferred location of the optimal as the time interval of optimal growth is increased. Changes in the structure and e-folding time of the fastest-growing mode, however, are not nearly so marked.

Based on the optimals of Gulf Stream flows that are stationary in time, one might be inclined to suggest that the flow field of Fig. 1 is inherently less predictable in the region of the large meander M2, since it is here that errors in the initial conditions can achieve maximum growth over a wide range of optimal-growth times. However, if we take into account the temporal variation of the basic state, then based upon the energy optimal found in section 7, with most rapid energy growth over 4 days, we would be inclined to suggest that the meander M1 is the most unpredictable feature in the model. For the time-evolving flow studied, eddy formation appears to stabilize the flow with respect to optimal perturbation growth, while eddy merger events appear to destabilize the flow. Clearly, further work is required to elucidate the predictability of such flow fields using the spectrum of optimal perturbations.

TABLE 3. A selection of e-folding times for Gulf Stream meanders calculated in other theoretical, modeling, and observational studies.

Source	e-folding time (days)	Comments
Hauriwitz and Panofsky (1950)	0.7	Barotropic instability only
Lipps (1963)	3.8	Barotropic instability only
Tareev (1965)		Baroclinic instability only:
	2.6	Frictionless
	4.0	With friction
Orlanski and Cox (1973)		Baroclinic instability only:
	0.6–3.0	Linear analysis
	1.0–7.0	Nonlinear analysis with GCM
Tracey and Watts (1986)	4–30	From observation
Watts and Johns (1982)	6–14	From observation (uncertainty ±50%).

However, the results presented here illustrate not only the wealth of information available from the tangent linear model and its adjoint, but also the potential importance of analyzing time-varying basic states.

While the computational cost of a complete investigation of the predictability of oceanic flows using the current iterative method is prohibitive, and while our conclusions are somewhat specific to the example studied, we believe that adjoint models are potentially very powerful multipurpose modeling tools that should be actively developed by ocean prediction and numerical weather-prediction centers.

Finally, we note that the study of optimal perturbations can be used to place an upper bound on the growth rate of disturbances on geophysical flows. Table 3 presents a selection of estimates of the *e*-folding time for meanders on the Gulf Stream calculated theoretically from models or inferred from direct observations. As Table 3 shows, a wide range of *e*-folding times have been found for Gulf Stream meanders depending upon their spatial scale and their geographical location with respect to bottom topography. All of the modes and optimal perturbations investigated in this study have *e*-folding times (see Table 2) that lie in the range 0.7–3.0 days suggested by Table 3.

Acknowledgments. Andrew Moore gratefully acknowledges the support of the Australian Department of the Arts, Sport, the Environment, Tourism and Territories. Brian Farrell acknowledges the support of NSF ATM-8912432. We are very grateful to Professor Allan Robinson and the Harvard Oceanography Group for making their ocean model available to us. We are also grateful to Jorgen Frederiksen, Peter Baines, Roger Hughes, and Carlos Lozano for valuable discussions and comments regarding earlier versions of the manuscript. We are also grateful to two anonymous reviewers for their comments. All computations were performed on a CRAY Y-MP two processor supercomputer operated by Leading Edge Technologies, Port Melbourne, Australia.

REFERENCES

Arakawa, A., and V. R. Lamb, 1977: Computational design of the basic dynamical processes of the UCLA general circulation model. *Methods Comput. Phys.*, **17**, 173–265.

Charney, J. G., 1947: The dynamics of long waves in a baroclinic westerly current. *J. Meteor.*, **4**, 135–162.

——, R. Fjortoft, and J. von Neumann, 1950: Numerical integrations of the barotropic vorticity equation. *Tellus*, **2**, 237–254.

——, R. G. Fleagle, H. Riehl, V. E. Lally, and D. Q. Wark, 1966: The feasibility of a global observation and analysis experiment. *Bull. Amer. Meteor. Soc.*, **47**, 200–220.

Courant, R., and D. Hilbert, 1962: *Methods of Mathematical Physics. Vol. 2.* Wiley-Interscience, 830 pp.

Eady, E. T., 1949: Long waves and cyclone waves. *Tellus*, **1**, 33–52.

Farrell, B. F., 1985: Transient growth of damped baroclinic waves. *J. Atmos. Sci.*, **42**, 2718–2727.

——, 1987: Developing disturbances in shear. *J. Atmos. Sci.*, **44**, 2191–2199.

——, 1988: Optimal excitation of neutral Rossby waves. *J. Atmos. Sci.*, **45**, 163–172.

——, 1989: Optimal excitation of baroclinic waves. *J. Atmos. Sci.*, **46**, 1193–1206.

——, 1990: Small error dynamics and the predictability of flows. *J. Atmos. Sci.*, **47**, 2409–2416.

——, and A. M. Moore, 1992: An adjoint method for obtaining the most rapidly growing perturbation to oceanic flows. *J. Phys. Oceanogr.*, **22**, 338–349.

Fix, G. J., 1975: Finite element models for ocean circulation problems. *SIAM J. Appl. Math.*, **29**, 371–387.

Frederiksen, J. S., 1982: A unified three-dimensional theory of the onset of blocking and cyclogenesis. *J. Atmos. Sci.*, **39**, 970–982.

——, 1986: Instability theory and non-linear evolution of blocks and mature anomalies. *Advances in Geophysics*, Vol. 29, Academic Press, 277–303.

——, 1989: The role of instability during the onset of blocking and cyclogenesis in Northern Hemisphere synoptic flows. *J. Atmos. Sci.*, **46**, 1076–1092.

——, and P. J. Webster, 1988: Alternative theories of atmospheric teleconnections and low-frequency fluctuations. *Rev. Geophys.*, **26**, 459–494.

Gill, A. E., 1982: *Atmosphere-Ocean Dynamics.* Academic Press, 662 pp.

——, J. S. Green, and A. J. Simmons, 1974: Energy partition in the large-scale ocean circulation and the production of mid-ocean eddies. *Deep-Sea Res.*, **21**, 499–528.

Haidvogel, D. B., A. R. Robinson, and E. E. Schulman, 1980: The accuracy, efficiency and stability of three numerical models with application to open ocean problems. *J. Comput. Phys.*, **34**, 1–53.

Hauriwitz, B., and H. A. Panofsky, 1950: Stability and meandering of the Gulf Stream. *Trans. Amer. Geophys. Union*, **31**, 723–731.

Hoffman, R. N., and E. Kalnay, 1983: Lagged average forecasting, an alternative to Monte Carlo forecasting. *Tellus*, **35A**, 100–118.

Holland, W. R., and D. B. Haidvogel, 1980: A parameter study of the mixed instability of idealized ocean currents. *Dyn. Atmos. Oceans*, **4**, 185–215.

Ikeda, M., 1981: Meanders and detached eddies for a strong eastward-flowing jet using a two-layer quasigeostrophic model. *J. Phys. Oceanogr.*, **11**, 526–540.

Joly, A., and A. J. Thorpe, 1991: The stability of time-dependent flows: An application to fronts in developing baroclinic waves. *J. Atmos. Sci.*, **48**, 163–182.

Killworth, P. D., 1980: Barotropic and baroclinic instability in rotating stratified fluids. *Dyn. Atmos. Oceans*, **4**, 143–184.

Lacarra, J., and O. Talagrand, 1988: Short-range evolution of small perturbations in a barotropic model. *Tellus*, **40A**, 81–95.

Le Dimet, F., and O. Talagrand, 1986: Variational algorithms for analysis and assimilation of meteorological observations: Theoretical aspects. *Tellus*, **38A**, 97–110.

Lipps, F. B., 1963: Stability of jets in a divergent barotropic fluid. *J. Atmos. Sci.*, **20**, 120–129.

Lorenz, E. N., 1965: A study of the predictability of a 28-variable atmospheric model. *Tellus*, **17**, 321–333.

——, 1969a: The predictability of a flow which possess many scales of motion. *Tellus*, **21**, 289–307.

——, 1969b: Atmospheric predictability as revealed by naturally occurring analogues. *J. Atmos. Sci.*, **26**, 636–646.

——, 1982: Atmospheric predictability experiments with a large numerical model. *Tellus*, **34**, 505–513.

Miller, R. N., A. R. Robinson, and D. B. Haidvogel, 1981: A baroclinic quasi-geostrophic open ocean model. *J. Comput. Phys.*, **50**, 38–70.

MODE Group, 1978: The Mid-Ocean Dynamics Experiment. *Deep-Sea Res.*, **25**, 859–910.

Moore, A. M., 1991: Data assimilation in a quasigeostrophic open-ocean model of the Gulf Stream region using the adjoint method. *J. Phys. Oceanogr.*, **21**, 398–427.

Orlanski, I., and M. D. Cox, 1973: Baroclinic instability in ocean currents. *Geophys. Fluid Dyn.*, **4**, 297–332.

Palmer, T. N., 1988: Medium and extended-range predictability and stability of the Pacific. North American mode. *Quart. J. Roy. Meteor. Soc.*, **114**, 691–713.

Pedlosky, J., 1964: The stability of currents in the atmosphere and the ocean: Part I. *J. Atmos. Sci.*, **21**, 201–219.

——, 1979: *Geophysical Fluid Dynamics.* Springer-Verlag, 624 pp.

Petterssen, S., and S. Smebye, 1971: On the development of extra-tropical cyclones. *Quart. J. Roy. Meteor. Soc.*, **97**, 457–482.

Robinson, A. R., and J. C. McWilliams, 1974: The baroclinic instability of the open ocean. *J. Phys. Oceanogr.*, **4**, 281–294.

——, and L. J. Walstad, 1987: The Harvard Open Ocean Model: Calibration and application to dynamical process, forecasting, and data assimilation studies. *Appl. Numer. Math.*, **3**, 89–131.

——, M. A. Spall, and N. Pinardi, 1988: Gulf Stream simulations and the dynamics of ring and meander processes. *J. Phys. Oceanogr.*, **18**, 1811–1853.

——, ——, L. J. Walstad, and W. G. Leslie, 1989a: Data assimilation and dynamical interpolation in GULFCAST experiments. *Dyn. Atmos. Oceans*, **13**, 301–316.

——, S. M. Glenn, M. A. Spall, L. J. Walstad, G. M. Gardiner, and W. G. Leslie, 1989b: Forecasting Gulf Stream meanders and rings. *Eos, The Oceanography Report*, **70**(45), 1464–1473.

Shapiro, R., 1970: Smoothing, filtering, and boundary effects. *Rev. Geophys. Space Phys.*, **8**, 359–386.

Tareev, B. A., 1965: Unstable Rossby waves and the instability of oceanic currents. *Izv. Acad. Sci. USSR Atmos. Oceanic Phys.*, **1**, 426–438.

Thacker, W. C., 1990: Large least-square problems and the need for automating the generation of adjoint codes. *Lect. Appl. Math.*, 26, *Computational Solution of Nonlinear Systems of Equations*, Amer. Math. Soc., 645–677.

Tracey, K. L., and D. R. Watts, 1986: On Gulf Stream meander characteristics near Cape Hatteras. *J. Geophys. Res.*, **91**, 7587–7602.

Watts, D. R., and W. E. Johns, 1982: Gulf Stream meanders: Observation on propagation and growth. *J. Geophys. Res.*, **87**, 9467–9476.

Valdes, P. J., and B. J. Hoskins, 1988: Baroclinic instability of the zonally averaged flow with boundary-layer damping. *J. Atmos. Sci.*, **45**, 1584–1593.